CHALMERS

Design of an axial flux machine for an in-wheel motor application

Master of Science Thesis

CHRISTIAN DU-BAR

Department of Energy and Environment
Division of Electric Power Engineering
CHALMERS UNIVERSITY OF TECHNOLOGY
Göteborg, Sweden, 2011

Design of an axial flux machine for an in-wheel motor application

CHRISTIAN DU-BAR

Department of Energy and Environment
Division of Electric Power Engineering
CHALMERS UNIVERSITY OF TECHNOLOGY
Göteborg, Sweden, 2011

Design of an axial flux machine for an in-wheel motor application

Examiner:

Sonja Lundmark
Department of Energy and Environment
Chalmers University of Technology
SE-412 96 Göteborg
Sweden

Supervisor:

Joachim Lindström
Volvo Technology

Chalmers Reproservice
Göteborg, Sweden 2011

Abstract

This master thesis deals with the design of an axial flux machine for an in-wheel motor application. Four double-sided axial flux machine topologies are compared to select the most suitable one for designing a high torque density machine that fits into a predefined geometry (diameter: 260 mm, length: 72.5 mm). The yokeless and segmented armature (YASA) topology is chosen, due to its very compact structure. The design is made by using analytic and 3D finite element analysis alternately.

The geometry of the electromagnetic circuit is optimized to find the maximum rated torque (≈80 Nm) for proposed values of magnetic flux and current densities (1.7 T and 7 A/mm^2). These densities are chosen with the intension of reaching a high utilization of both the copper and the iron in the machine, when their proportions are determined by the maximal product of electric and magnetic loading.

When the geometry of the electromagnetic circuit is determined, it is held fixed. Possible different torque speed characteristics of the machine are then investigated, with respect to current and voltage limitations together with the turn selections of the windings.

A final design is proposed and its theoretical characteristics are evaluated and presented. The power density, at 2400 rpm and 7 A/mm^2, is calculated to 5.3 W/cm^3. Furthermore, some suggestions for future work and modifications are made.

Acknowledgements

This master thesis started in late autumn 2010 at Volvo Technology and was continued at Chalmers University of Technology during the spring of 2011. I am very grateful to the experienced and helpful persons that I have met during this time and I express extra thanks to:

Joachim Lindström, my supervisor, provided great support and guidance during the whole project. Sonja Lundmark, my examiner, for valuable advice and feedback regarding the report. Martin West, Volvo Technology, who shared clever ideas about electric machine design as well as a very positive attitude. Maddalena Cirani, Volvo Technology, for advice about axial flux machines. Johan Åström, Chalmers University of Technology, who generously shared his experience of FEA and electric machine modeling. Stefan Lundberg, Chalmers University of Technology, for time spent discussing and answering my questions about the machine modeling in the dq-coordinate system. Magnus Dahlström, Höganäs, for supply of data for SMC materials.

Christian Du-Bar
Göteborg, Sweden
June, 2011

Contents

Abbreviations

AC	alternating current
AFM	axial flux machine
AFIR	axial flux internal rotor
AFIS	axial flux internal stator
BLDC	brushless direct current
DC	direct current
FEA	finite element analysis
FFT	fast Fourier transform
PM	permanent magnet
PMSM	permanent magnet synchronous machine
YASA	yokeless and segmented armature

Symbols

Latin		
A	area	m^2
B	magnetic flux density	T
$\hat{B}_1$	fundamental magnetic flux density peak	T
D_i	inner air gap diameter	m
D_o	outer air gap diameter	m
f	frequency	Hz
f_{el}	electric frequency	Hz
H	magnetic field strength	A/m
H_c	magnetic coercivity	A/m
I_{ph}	phase current rms	A
J	current density rms	$\mathrm{A/m}^2$
k_d	distribution factor	
k_p	pitch factor	
k_w	winding factor	
$K_{cu-fill}$	copper fill factor	
l	length or thickness	m
l_g	air gap length	m
l_{pm}	permanent magnet length	m
l_r	rotor back thickness	m
L	inductance	H
L_d	direct-axis inductance	H
L_q	quadrature-axis inductance	H
m_1	number of phases	
m_a	amplitude modulation ratio	
n	number of turns per stator segment, index of harmonics	
N_{ph}	number of turns per phase	
N_s	number of stator segments	
P	power	W
p	number of pole pairs	
R	resistance	Ω
R_i	inner air gap radius	m
R_o	outer air gap radius	m
T	torque	Nm
U	voltage	V
U_{dc}	dc-link voltage	V
z	number of coils in a group	

Greek

ϕ	magnetic flux	Wb
λ	ratio between inner and outer diameter	
ω	mechanical angular frequency	rad/s
ω_{el}	electrical angular frequency	rad/s
ω_w	wheel angular frequency	rad/s
ψ_m	magnetic flux linkage due to permanent magnets	Wb
μ	permeability	H/m
μ_0	vacuum permeability	H/m
$\mu_{r,pm}$	relative permeability of permanent magnets	
σ	conductivity	S/m
σ_{cu}	copper conductivity	S/m
η	efficiency	

1 Introduction

1.1 Background

The last years' cold winters have caused problems in the traffic when heavy duty vehicles have been stuck on slippery roads with traffic congestion as a consequence. European regulations require that at least 25% of the total weight of the vehicle is carried by driving axles [1]. If electric motors are added to axels that do not receive torque from the existing drive train, it may be possible to reduce the number of vehicles stuck with spinning wheels and also to make sure that the regulations are fulfilled.

Another interesting possibility when electric machines are added to the vehicles is that the drive cycle for the existing drive train can be made smoother. The electric machines can be used for power assistance when going uphill and for regenerative breaking when going downhill. This may lead to an increased average speed, lowered fuel consumption and thereby also reduced impact on the environment and cost savings.

The axial flux permanent magnet machine is very interesting for vehicle applications due to its short axial length together with the high efficiency, when using permanent magnets. It can be engine integrated but the efficiency can be further increased if the drive train is minimized. When suitable, regarding the machine size and torque demand, direct driven in-wheel motors without gears can be used to improve the efficiency, lower the maintenance and offer independent control of each wheel [2].

1.2 Previous work

Volvo 3P is interested in electrical wheel motors for trucks in long-haul applications and financed a feasibility study during 2008-2009. An initial study to investigate potential performance improvement and a rough evaluation of the available space inside the rim was carried out by Volvo Technology [3].

A planetary gear with a gear ratio, of 6:1 to 10:1, was proposed to reduce the torque requirements of the electric machine, since the torque production is strictly limited by its volume. On the other hand the torque rating of the planetary gear is directly influenced by its own size or volume and the gear ratio is thereby also limited.

Different motor types were considered, permanent magnet and switched re-

luctance machines become the most interesting candidates due to their high torque density and high efficiency. The permanent magnet machine was finally chosen as most suitable for the application due to higher torque density, lower torque ripple and not so critically small air gap needed.

A DC-link voltage of 600 V from the battery is used. Variations of ± 100 V depending on the state-of-charge and load should be considered. It was also indicated that an increase of the DC-link voltage was of interest.

There are no fixed requirements of power and torque ratings for the machine but the performance investigation in [3] indicates the following targets for one machine:

- $P_{max} \approx 50 - 70$ kW
- $T_{max} \approx 400$ Nm
- $V_{DC-min} = 500$ V

Detailed investigations of possible mechanical solutions for integrating an electrical motor into the front wheel of a truck, were made as a master thesis during 2010 [4]. Two final concepts, one to fit a radial flux machine and one to fit a transverse flux machine were stated. The radial flux machine solution requires more changes of the existing hub configuration than the more compact transverse flux machine solution does. Due to known issues regarding the power factor of transverse flux machines, the very compact hub concept originally designed for a transverse flux machine is considered for this design of an axial flux machine, see Figure 1.

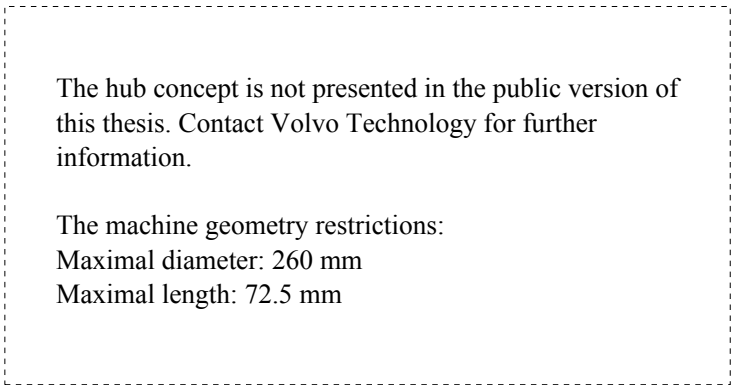

Figure 1: Available space for the electric machine and the power electronics.

1.3 Objective

The objective is to design an electrical axial flux permanent magnet machine that fits into the limited space specified and, if possible, meets the targets indicated. If it is not achieved, the obtained maximum power and torque ratings should be presented.

1.4 Scope

This master thesis combines analytic design and finite element analysis (FEA) based design of an axial flux permanent magnet machine. As it is difficult to carry out a complete and accurate analytic design, in comparison with a radial flux machine, FEA and analytic calculations are used alternately during the design process. The analytic part is used to speed up the process, calculate initial values etc., but also to verify the FEA solutions and to make appropriate decisions about modifications. In general, the design process is an iterative process which may be looped several times before a satisfactory solution is reached.

Before the design process starts, some basic theory about permanent magnet machines is presented. Four variations of two major topologies (internal rotor double stator and internal stator double rotor) are compared to find the most suitable one for the given requirements.

The design process can be subdivided into the following steps:

- Selection of topology
- Selection of pole number
- Optimization of the electromagnetic design
  - Analytic before choice of material
  - FEA after choice of material
- Investigation of torque speed characteristic
- Evaluation

2 Axial flux permanent magnet machines

The geometries of the permanent magnet axial flux machines in this report are described in the cylindrical coordinate system shown in Figure 2. The machine geometry lies centralized around the z-axis and the rotational parts rotate around the z-axis in the $\pm\theta$-direction. The axial length is in the z-direction, which is also called the axial direction. The machine quantities are described in the radial direction, which is a direction from the z-axis that is parallel to the xy-plane.

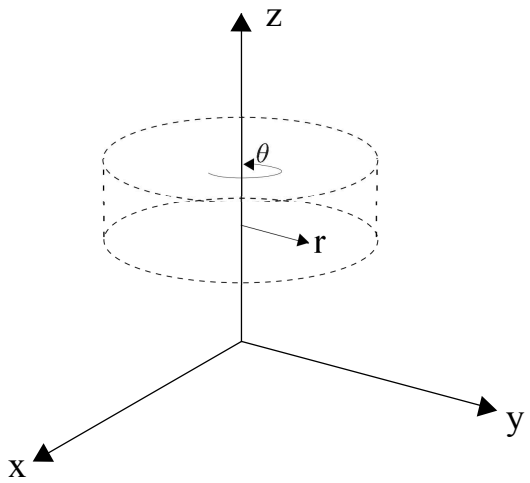

Figure 2: Axial flux machine in a cylindrical coordinate system.

2.1 Principles of permanent magnet machines

2.1.1 Torque production

The electrodynamic torque in an electric machine can be derived starting from the Lorentz force [5] [6]. This is the force acting on a charge, q that moves with velocity, $\boldsymbol{v}$, in a magnetic field, $\boldsymbol{B}$:

$$\boldsymbol{F}_q = q(\boldsymbol{v} \times \boldsymbol{B}) \tag{1}$$

If several charges are moving in a conductor, (1) can be rewritten as:

$$d\boldsymbol{F} = Id\boldsymbol{l} \times \boldsymbol{B} \tag{2}$$

where $d\boldsymbol{F}$ is the force acting on an infinitely small line-segment, $d\boldsymbol{l}$, carrying the line-current, I, in the field, $\boldsymbol{B}$, see Figure 3a.

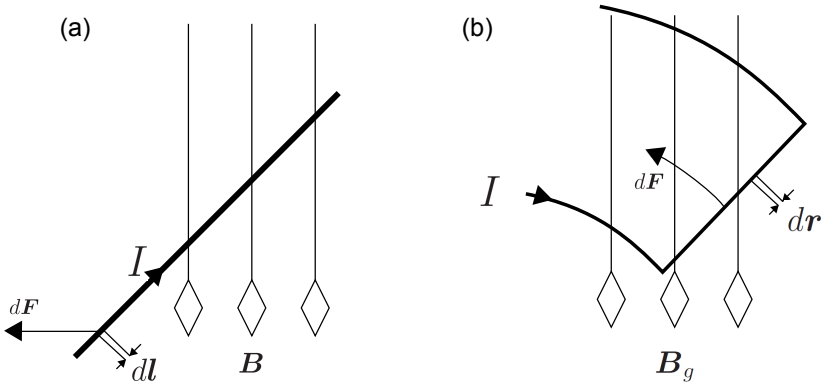

Figure 3: Force on current carrying conductors in a magnetic field.

The geometry of a segment of a conductor in an axial flux machine is shown in Figure 3b. The magnetic field in the air gap, $\boldsymbol{B}_g$, is oriented in the axial direction and assumed to be constant. Only the conductor part in the radial direction is of interest, as the force of interest is in the θ-direction, (2) can therefore be rewritten as:

$$dF_\theta = Idr \cdot B_g \tag{3}$$

Hence, the torque on each conductor segment is

$$dT_\theta = rdF_\theta = rIdr \cdot B_g \tag{4}$$

where r is the distance from the rotor centrum. In the literature, Idr is often expressed as $A(r)dS$, where $A(r)$ is called the electric loading, which is defined as the sum of the currents in all the conductors spread over a circle with the radius r.

$$A(r) = \frac{m_1 N_{ph} I_{ph}}{\pi r} \tag{5}$$

where m_1 is the number of phases, N_{ph} is the number of conductors in each phase and I_{ph} is the phase current.

An average air gap flux density, B_{g-avg}, together with (4) and (5) are then integrated from the inner radius of the air gap, $R_i = D_i/2$, to the outer radius of the air gap, $R_o = D_o/2$, with respect to r, [5]. The total average

torque from one rotor disc, when starting from the Lorentz force, becomes:

$$T_{avg} = \frac{1}{4} m_1 N_{ph} k_{w1} B_{g-avg} D_o^2 (1 - \lambda^2) I_{ph} \tag{6}$$

where k_{w1} is the winding factor of the fundamental and λ is the fraction of the outer and inner diameter ($\lambda = \frac{D_i}{D_o}$).

Another common approach to calculate the electromagnetic force on the rotor, shown in [5] and [7], is the product of the magnetic and electric loading $B_{g-avg} A(r = R_i)$ multiplied by the active surface S. For a double-sided machine $S = 2\pi(R_o^2 - R_i^2)$ and the average electromagnetic torque hence:

$$T_{avg-double} = 2\pi B_{g-avg} A(r = R_i)(R_o^2 - R_i^2) R_i \tag{7}$$

which also can be written as:

$$T_{avg-double} = 2\pi B_{g-avg} A(r = R_i) R_o^3 (\lambda - \lambda^3) \tag{8}$$

Starting from (8), taking the first derivative with respect to λ and equating it to zero, one can show that the maximum torque should be received for $\lambda = \frac{1}{\sqrt{3}}$. In practice it has been shown that the maximum torque is given for $\lambda \neq \frac{1}{\sqrt{3}}$, [5],[7].

2.1.2 Wave forms

Permanent magnet machines are often divided into permanent magnet synchronous machines (PMSM) and brushless direct current (BLDC) machines depending on their wave form characteristics. The back-EMF and the current wave form of a PMSM, sometimes called brushless AC machine, should ideally be perfectly sinusoidal. For an ideal BLDC machine, the back-EMF should be square or trapezoidal shaped and the currents to produce constant torque should be square shaped.

In Figure 4, the wave forms are explained considering a BLDC machine since its discretized characteristic may be easier to follow.

The air gap flux density produced by the permanent magnets is assumed to be quasi-square, as illustrated in Figure 4a. The magnet width corresponds to 2/3 of a pole pitch.

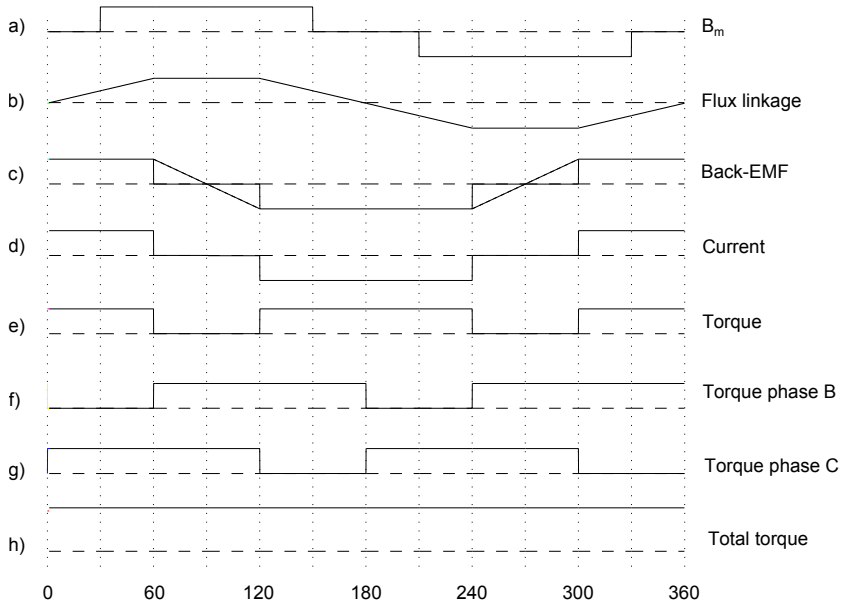

Figure 4: Ideal wave forms of a BLDC machine.

The permanent magnet flux linkage, ψ_m, is defined as the magnetic flux from the permanent magnets linking a winding. In Figure 4, a winding covers 60 degrees and the flux linkage can be expressed as:

$$\psi_m(\theta) = \int_{\theta-30}^{\theta+30} B_m(\theta)\,\mathrm{d}\theta \tag{9}$$

The back-EMF wave form can be determined by Faraday's Law, which states that the induced voltage equals the time derivative of the flux linkage:

$$e = \frac{\mathrm{d}\psi_m}{\mathrm{d}t} \tag{10}$$

which gives the square shaped back-EMF in Figure 4c.

DC-current is then switched on and off with the same polarity as the back-EMF, see Figure 4d. This gives a pulsating but always positive product that corresponds to the power and hence the torque produced by one phase, which is shown in Figure 4e.

For a three phase machine, the two remaining phases produce torque that is shifted 120 and 240 degrees respectively, see Figure 4f-g. Finally the torque

produced by the three phases sums up to the total torque produced by the machine, which is constant and two times the pulsating torque produced by one phase, see Figure 4h.

The sinusoidal flux linkage for a PMSM can be received by changing the discretized geometry of a BLDC machine. If the geometry is changed to form a perfect sinusoidal air gap flux density, the same discretized and concentrated winding configuration as for the BLDC machine can be used to get sinusoidal flux linkage. A sinusoidal flux linkage can also be received if the air gap flux density is kept square shaped but the windings are rearranged in a sinusoidal distribution. In practice, neither the air gap flux density nor the distribution of the windings are perfectly sinusoidal but they are combined to get as little harmonic content as possible for a PMSM.

The torque densities of a PMSM and a BLDC machine of the same sizes are compared by [8]. The iron losses of the two machines are assumed to be equal and the torque density limited by the thermal dissipation due to the copper losses. It was then shown that a BLDC machine could produce 15% more torque. On the other hand, the higher harmonic content of the square waves will contribute to the iron losses, and also cause extra copper losses due to less even current distribution and thereby probably affect the total losses significantly. The PMSM is expected to offer higher field weakening capability and less torque ripple [8].

2.1.3 Limiting factors

In the general case, electric machines are limited by thermal constraints. The torque or the power produced by a machine are thereby closely related to the ability to cool the machine. Most machines have capacity to manage a short time overload which may be several times higher than the rated torque depending on the time period that is considered. The permanent magnets and the insulation material of the windings are components that are sensitive to high temperature.

Another limiting factor is the mechanical aspect, a component in the electromagnetic circuit of a machine must often also provide mechanical support for the machine structure. Optimization of the electromagnetic circuit can thereby often result in a theoretic geometry that is of little or no practical use.

The permanent magnets could be demagnetized by a rise in temperature but also by the induced flux due to the current in the windings. This is of

particular interest when the machine is operating in field weakening, since the induced flux is directed against the flux from the permanent magnets.

2.2 Topologies

Several basic axial flux machine topologies exist, they can be divided into:

- Single-sided
- Double-sided internal rotor double stator
- Double-sided internal stator double rotor
- Multi-disc

It is also possible to subdivide them further depending on: winding configuration, slotted or slotless stator, iron core or coreless stator and rotor etc.

2.2.1 Single-sided

With the single sided topology it is possible to get a very high ratio between machine diameter and length, see Figure 5a. However, a significant attracting axial force between the rotor and the stator will appear and the force can not be balanced as for the other topologies where the outer rotors or stators are mechanically connected. The bearings must therefore be dimensioned to handle a greater axial force.

2.2.2 Double-sided internal rotor double stator

The internal rotor double stator topology is shown in Figure 5b and offers some extra reliability since it is able to operate with only one stator if the stators are connected in parallel. Preferably the stators are connected in series to better balance the axial forces [5]. The stator losses are distributed between the two stators and it may be easier to cool them by air. On the other hand, it may be more complex to implement liquid cooling in two stators. Theoretically, no rotor core is needed for this topology, as the magnetic flux path is only in the axial direction through the rotor.

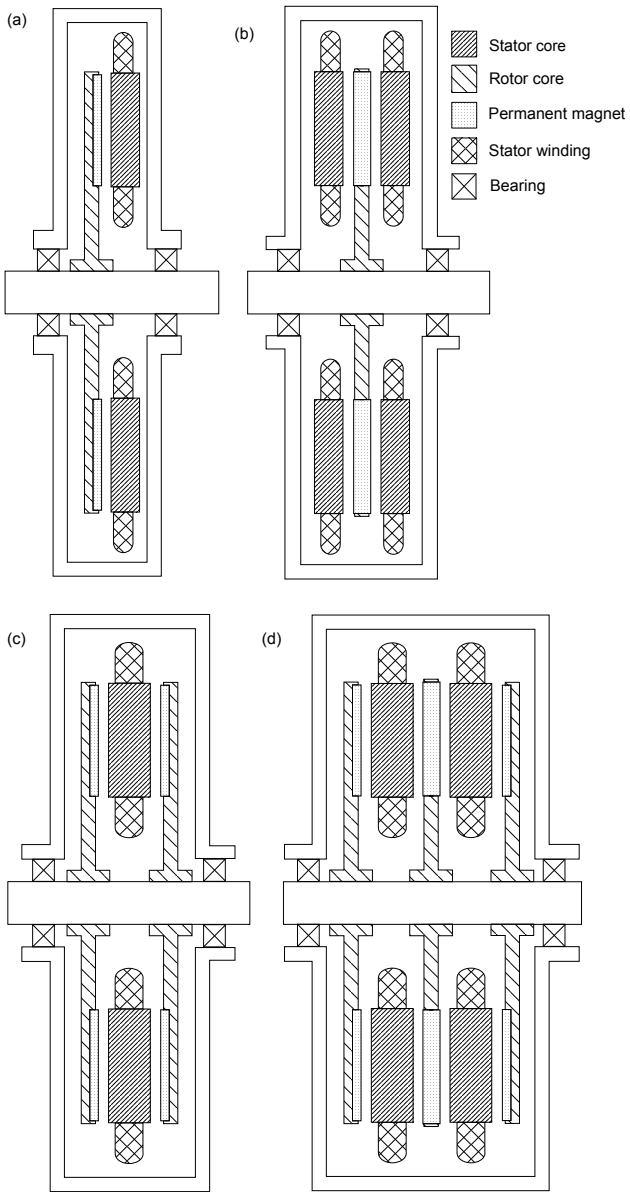

Figure 5: Four basic AFM topologies; a) Single-sided b) Double-sided internal rotor double stator c) Double-sided internal stator double rotor d) Multi-disc.

2.2.3 Double-sided internal stator double rotor

The axial forces can be balanced for the internal stator double rotor topology as well. As for the internal rotor double stator, there exists a corresponding design without a stator core, where the magnetic flux path through the stator

is in the axial direction only.

An interesting possibility of this basic topology is that the stator can be wound toroidally. If so, a stator core is needed since the flux must go in the θ-direction inside the stator.

2.2.4 Multi-disc

The increase of torque that can be achieved by enlarging the machine diameter can be limited by: axial force supported by bearings, mechanical joints between discs and shaft and the stiffness of the discs [5]. Instead, several rotor discs and stators can be added together to increase the torque, which is also a way of altering the ratio between machine length and diameter for axial flux machines. This topology could be interesting if there is available space left in the axial direction, when considering a double-sided machine.

2.3 Comparison of suitable topologies

Rough initial comparisons and calculations showed that neither the single-sided nor the multi-disc topologies were of interest for the specified ratio between diameter and length of the geometry. Four double-sided topologies with balanced axial forces are considered as the most suitable, and thus compared to motivate a final decision. The double-sided topologies to be studied further are: axial flux internal rotor (AFIR), toroidally wound internal stator (TORUS), axial flux internal stator (AFIS) and yokeless and segmented armature (YASA). Schematic figures of their respective flux paths and their distributions of the main parts can be seen in Figure 6.

All four topologies have some differences and some similarities. The similarities between TORUS, AFIS and YASA may be obvious as both TORUS and YASA can be said to be variations of AFIS.

The required axial length for the TORUS machine is greater than for the other topologies due to the extra flux path in the θ-direction, see Figure 6b. Ideally, the flux in the axial direction is zero in the middle of the stator and it is thereby possible to introduce a channel for fluid cooling inside the stator.

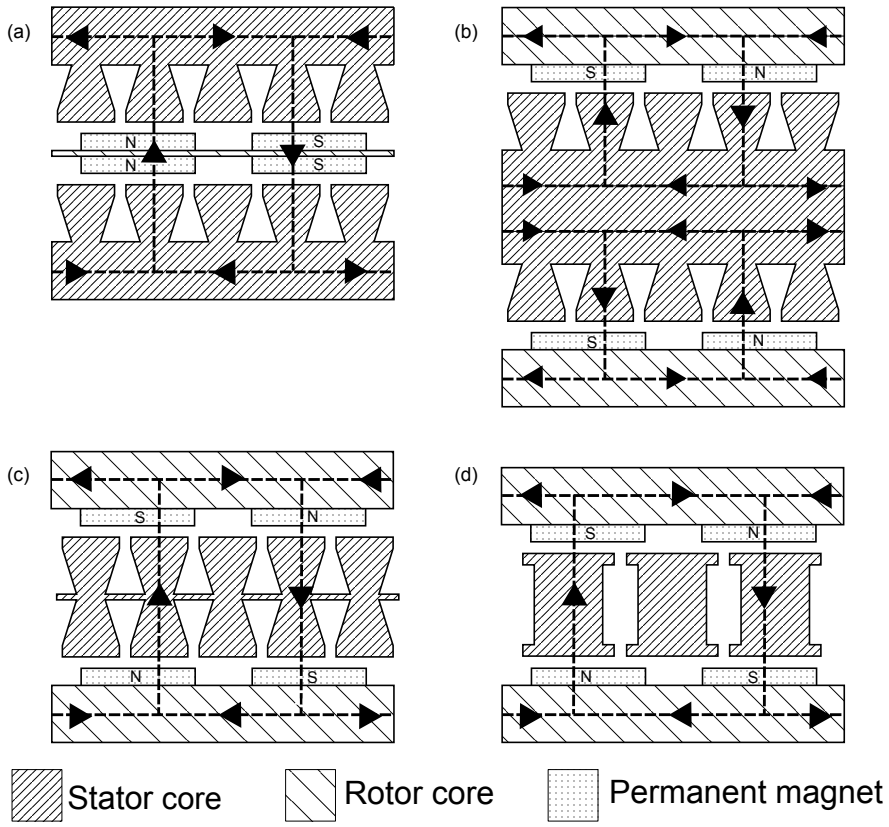

Figure 6: Schematic figures of the flux paths and distributions of a) AFIR, b) TORUS and c) AFIS d) YASA in axial direction.

The YASA topology can also be said to be a special case of the AFIS topology where the inter-polar stator core is eliminated, see Figure 6d. The first YASA motors were developed in 2007, using stator segments of powdered iron material, for the Morgan LIFEcar project[1] and presented by [9]. In 2008 a prototyped machine with laminated stator segment was presented by [2].

Schematic figures of the four topologies, to visualize the composition of the main parts in the radial direction, using an axial cut are shown in Figure 7. The protrusion of the end windings are expected to be greater for the AFIR and AFIS topologies [10], see Figure 6a and 6c. A TORUS machine is expected to require less space for the end windings as it is toroidally wound [7], [11]. For the YASA topology it is possible to shape the stator segment shoes to hide the windings and thereby maximize the diameter of the active

[1]Morgan LIghtweight Fuel Efficient Car, a project that aimed at producing the world's first hydrogen powered electric sports car.

area of the air gap, see Figure 7d.

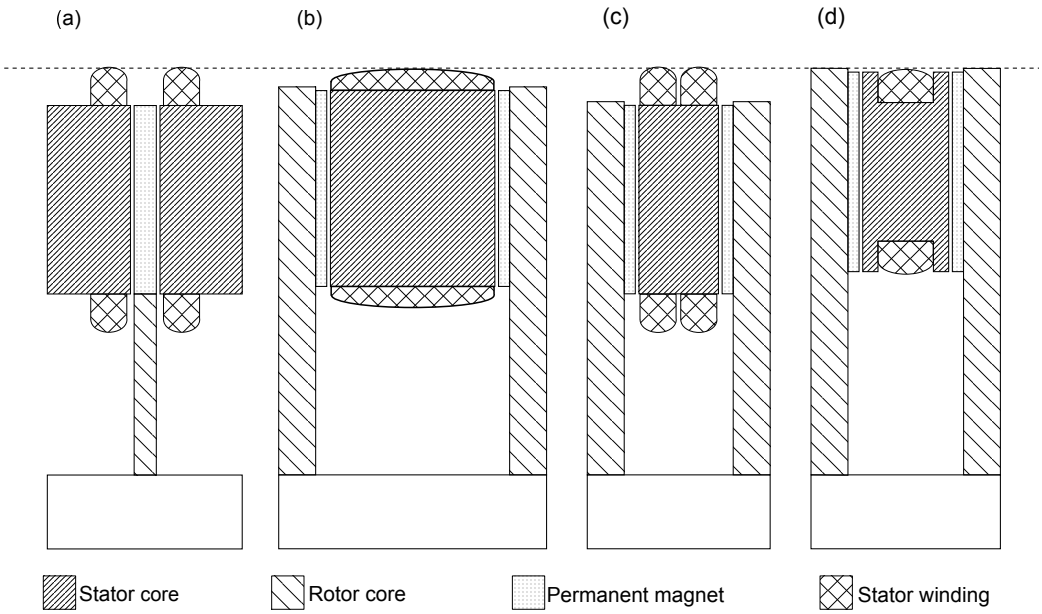

Figure 7: Schematic figures of the distributions of a) AFIR, b) TORUS and c) AFIS d) YASA in the radial direction.

As presented in section 2.1.1, the torque produced by an axial flux machine is stated to be proportional both to the square, (6), and to the cube, (7), of the air gap outer diameter. In Figure 8, the torque produced by a machine with an outer diameter of 260 mm is put to 1 pu. The outer diameter is then reduced as function of the end winding protrusions in the radial direction; 5 mm of end winding protrusion reduces the outer diameter by 10 mm. The figure shows the importance of maximizing the outer diameter (minimizing end winding protrusion) and the impact of the two different relations between the outer diameter and the torque.

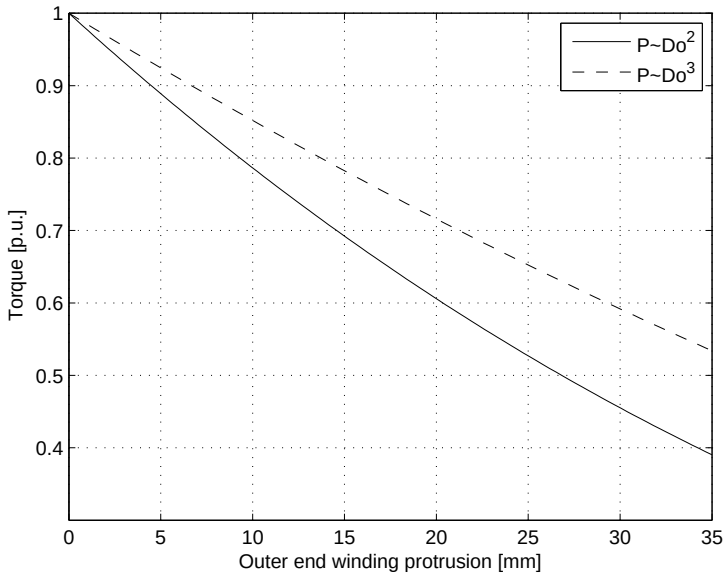

Figure 8: Torque production as function of end winding protrusion.

An attempt to compare the four topologies based on existing analytic designs was carried out early in this work. This was problematic since it was difficult to find reasonable values for the end winding protrusion without going into details, such as pole numbers and winding configurations etc. As four parallel machine designs were out of scope for this thesis, the expected properties and consequences for the four topologies are instead, somewhat simplified, summarized in Table 1.

Table 1: Expected distribution of the main parts along radial and axial directions for TORUS, AFIS, AFIR and YASA.

Radial	**TORUS**	**AFIS**	**AFIR**	**YASA**
End windings	Shorter end windings are expected for toroidal windings wound around the stator core.	Longer protrusion of the end windings is expected for conventional windings wound around the stator teeth.		The end windings are more or less hidden behind the stator shoes.
Stator	The outer radius of the stator is limited by the end winding protrusion inside a given machine radius.			The dimension of the stator shoes in the radial direction is limited by the space needed to avoid flux leakage to the casing.
Rotor core	Generally, a rotor core (or the material in between the PMs for AFIR) has the same dimensions as the active area or the air gap in the radial direction.			
Axial	**TORUS**	**AFIS**	**AFIR**	**YASA**
Stator core	A stator core is needed for the magnetic flux path in the θ-direction. Ideally the magnetic flux should be zero in the axial direction in the middle of the stator core.	Ideally, no stator core is needed; the teeth can be mounted back to back since the magnetic flux path should be in the axial direction only.	A stator core is needed for the magnetic flux path in the θ-direction.	The stator consists of segments without a magnetic connection in between. The needed length of the segments is influenced by the amount of copper in the machine.
Stator teeth	The lengths of the stator teeth are influenced by the electric loading and the amount of copper. The expected shorter end windings of the TORUS topology may indicate that it should be possible to make the stator slot and teeth configuration tighter as well.			The length of the stator shoes is influenced by the cross-sectional area of the central bar inside the stator segments.
Rotor core	A rotor core is needed for the magnetic flux in the θ-direction. Its thickness or its axial length is depending on both the material properties and the magnetic flux density, which together should be chosen to avoid saturation in the rotor core.		Ideally, no rotor core is needed since there is no flux path in the θ-direction.	The same case as for the TORUS and AFIS topologies.
Air gap	All the double-sided topologies include two air gaps, their length is mechanically restricted by the desired tolerance of vibrations and bending forces.			
PM	The total axial length of the permanent magnets is mainly depending on the total axial lengths of the air gaps.			

2.3.1 Selection of topology

Both the basic AFIR and AFIS topologies are well proven topologies but the space needed for the end windings in both cases is expected to significantly limit their torque production. For a machine with a diameter of 260 mm, 10 mm of end winding protrusion in both ends of the active area decreases the outer air gap diameter by 20 mm. The torque is then reduced to 80-85% compared to a theoretic machine where the diameter is fully utilized, see Figure 8.

The TORUS topology is expected to utilize the machine diameter better due to its more compact end windings. On the other hand an extra flux path in the θ-direction is introduced and the machine length is less effectively utilized.

Finally the YASA topology is expected to offer both the advantage of high torque and a compact machine. Using stator segments of soft magnetic composite (SMC), the stator segment shoes can overlap the windings and maximize the diameter of the air gap. The iron in the stator can typically be reduced to 50%, causing a torque density increase of around 20% when compared to other axial flux machines [9].

When comparing the targets in terms of torque, power and the available space for this design with the performance of other existing machines, it is obviously a very demanding combination. Therefore the compact YASA topology is considered the most interesting topology and chosen for this specific design.

3 Analytic models

Various analytic design methods, empirically developed, can be found in scientific papers. Some of them are used for calculations to obtain an initial approximate solution, to be further analyzed using finite element analysis (FEA). Others are more accurate and based on lumped parameter magnetic circuits, which can take 3D-geometry into account [12].

3.1 Machine characteristics in the dq-coordinate system

The machine characteristics can be derived starting from the equivalent circuit of a PMSM, described in the dq-coordinate system, as shown in Figure 9. Amplitude invariant peak transformation is used and as a consequence all quantities are referred to phase peak values.

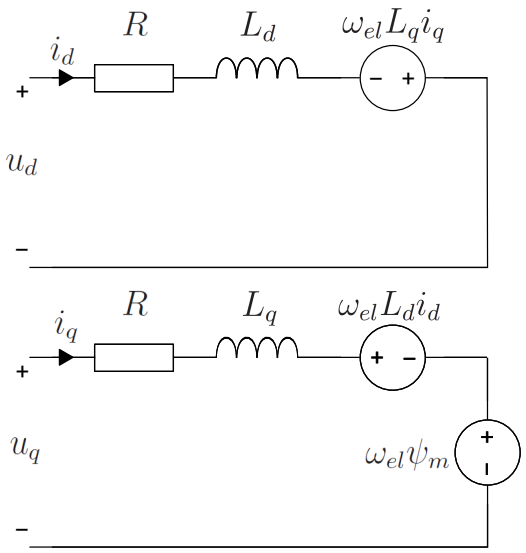

Figure 9: Dq-coordinate system equivalent PMSM circuit.

The expressions for the d- and q-components of the phase voltage for the dynamic model then become:

$$u_d = Ri_d + L_d \frac{di_d}{dt} - \omega_{el} L_q i_q \tag{11}$$

$$u_q = Ri_q + L_q \frac{di_q}{dt} + \omega_{el} L_d i_d + \omega_{el} \psi_m \tag{12}$$

The amplitude of the phase voltage is calculated as:

$$u = \sqrt{u_d^2 + u_q^2} \tag{13}$$

The time derivatives of the currents, in (11) and (12), are zero if a steady state is considered. If, in addition, the d- and q-axis inductances are assumed to be equal (L_d=L_q=L) and the phase resistance,R , is neglected, (11), (12) and (13) can be combined and rewritten as:

$$\left(\frac{u}{\omega_{el}L}\right)^2 = i_q^2 + \left(\frac{\psi_m}{L} + i_d\right)^2 \tag{14}$$

If the voltage, u, is considered as the maximal voltage available, (14) can be visualized as voltage limit circles in the $i_d i_q$-plane [13]; represented by the dashed circles in Figure 10. The circles' center point lies in $-\psi_m/L$ on the i_d-axle and their radii are inversely proportional to the electric angular frequency, ω_{el}, and given by $\frac{u}{\omega_{el}L}$.

The d- and q-components of the current can be used to calculate the amplitude of the phase current the same way as the phase voltage previously:

$$i = \sqrt{i_d^2 + i_q^2} \tag{15}$$

Again, if the current, i, is considered as the maximal current available, equation (15) can be visualized as a current limit circle which is centered in origo in the $i_d i_q$-plane.

The electrodynamic torque produced by a PMSM can generally be expressed as:

$$T = \psi_m i_q + (L_d - L_q) i_q i_d \tag{16}$$

As L_d and L_q are assumed to be equal (L_d=L_q=L), the reluctance torque term is zero. The remaining part of the torque is then proportional to the q-component of the current, i_q, and simply expressed as:

$$T = \psi_m i_q \tag{17}$$

Constant torque can be visualized as horizontal lines in the $i_d i_q$-plane, represented by the dotted lines plotted in Figure 10.

A permissible operating point at a certain speed must lie both inside the current limit circle and inside the corresponding voltage limit circle in the $i_d i_q$-plane. When the center of the voltage limit circles, $-\psi_m/L$, lies inside the current limit circle or on its boundary as in Figure 10, the machine can in theory be operated at infinite speed. This since there will be a permissible operating point for any speed.

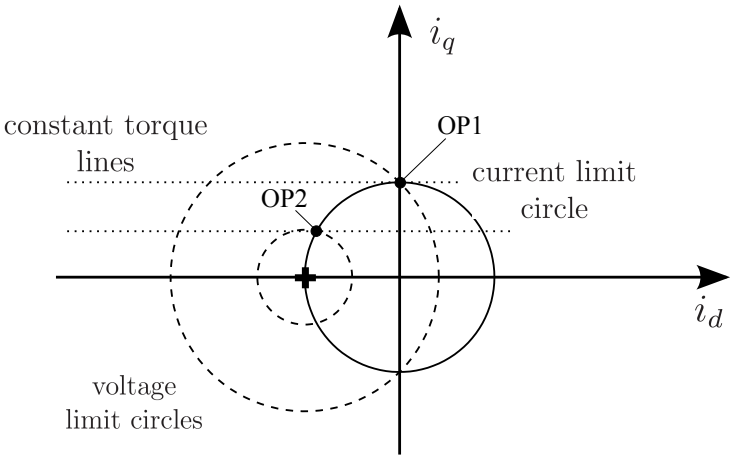

Figure 10: Current and voltage limit circles in the $i_d i_q$-plane.

The generalized torque speed characteristic of a machine with field weakening possibilities is shown in Figure 11. Starting from zero speed in the constant torque region, the machine is fed with $i_q = i_n$ and $i_d = 0$, which gives rated torque up to rated speed. The rated torque and rated speed operating point corresponds to OP1 in Figure 10.

To further increase the speed and to get the maximal possible torque at this speed, a negative d-component current, i_d, must be applied to follow the decreasing voltage limit circle. Hence, i_q must be reduced to stay in the current limit circle. OP2 in Figure 10 shows an example of a field weakening operation point for maximum torque.

The region beyond rated speed is often called constant power region but the power is changing since the increase of speed and the decrease of torque will not result in a constant power product.

$$P = T\omega \tag{18}$$

Voltage phasor diagrams are plotted for three different operating points in Figure 12. The phase displacements between the voltages and the currents are denoted by φ. For an infinite speed machine, it can be shown that the maximum power factor, $|cos(\varphi)|$, below rated speed is $\frac{1}{\sqrt{2}} = 0.71$. As φ decreases for speeds beyond rated speed, the power factor starts to increase in field weakening operation which can be seen in Figure 12c.

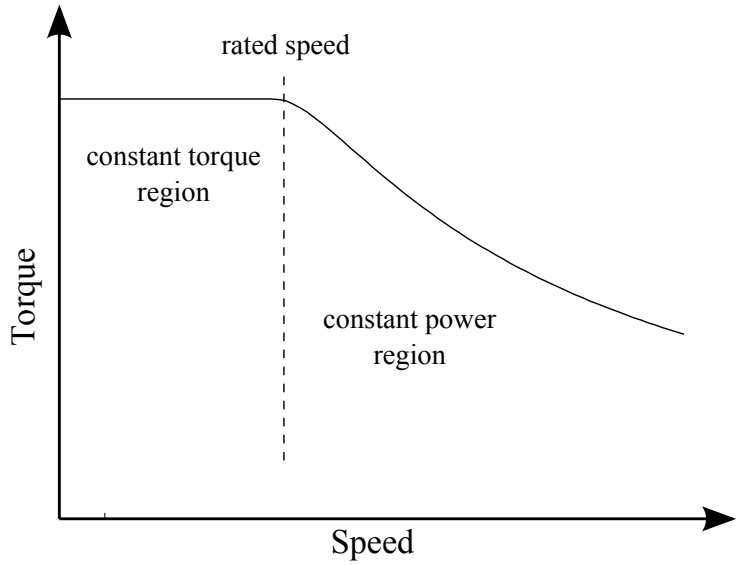

Figure 11: Generalized torque speed characteristics.

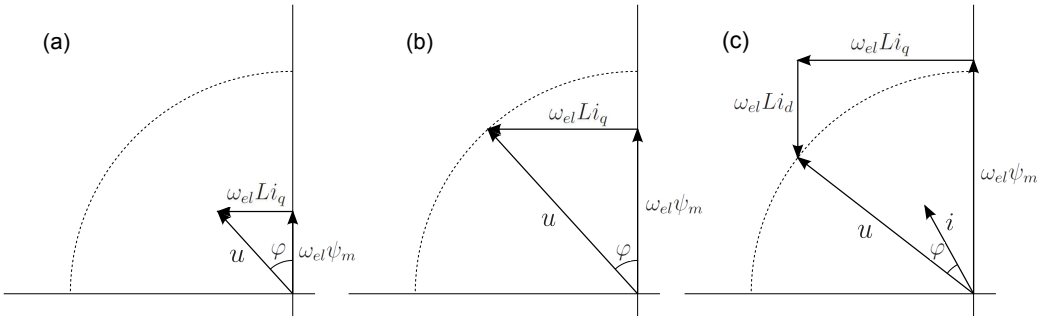

Figure 12: Voltage phasor diagrams: a) below rated speed, b) at rated speed, c) field weakening operation.

3.2 Voltage limit

The machine characteristics are evaluated for the phase voltage that corresponds to the minimum operational DC-link voltage of 500 V. For a three phase inverter, it can be shown that the maximum line-to-line rms voltage of the fundamental frequency can be written as :

$$U_{LL-1-rms} = \frac{\sqrt{3}}{2\sqrt{2}} m_a U_{DC} \tag{19}$$

where m_a is the amplitude modulation ratio and the linear region is defined as $m_a \leq 1$ [14]. By adding the 3rd harmonic to the phase voltage the linear range of modulation can be increased by 15%. The expression for the maximum phase peak voltage then becomes:

$$\hat{U}_{ph-1} = \frac{U_{DC}}{2} m_a \cdot 1.15 \tag{20}$$

3.3 Pole pairs and stator segment combinations

The total number of poles, $2p$, should be as close as possible to the number of stator segments, N_s, to maximize the magnetic flux linkage. Equal numbers can't be used if the motor is to be able to produce torque in all rotor positions. The feasible slot and pole number combinations are usually described by (21),

$$N_s = 2p \pm 1 \; or \; 2p \pm 2 \tag{21}$$

where N_s must be divisible by 3 for a three phase machine. The phase-shift angle, θ_{ps} in electrical degrees, must be $\pm 360k + 120$, where k is a positive integer [15],

$$\theta_{ps} = \beta_s \frac{N_s}{3} \frac{180}{\beta_p} = \frac{2p\beta_p}{N_s} \left(\frac{N_s}{3} \frac{180}{\beta_p} \right) = \frac{360p}{3} \tag{22}$$

where β_p is the magnet pole-pitch angle and $\beta_s = 2p\beta_p / N_s$ is the slot-pitch angle.

All possible combinations, up to p=16, derived from (21) and (22) are listed in Table 2. It can be noted in Table 2 that no combinations where p is divisible by 3 exist, which is a consequence of (21). N_s and p for a given combination of N_s/p can be multiplied by a positive integer to get a new

Table 2: Feasible pole and slot number combinations for a 3-phase machine.

Number of pole pairs, p	$\mathbf{N_s = 2p \pm 1}$	$\mathbf{N_s = 2p \pm 2}$
1	3	-
2	3	6
4	9	6
5	9	12
7	15	12
8	15	18
10	21	18
11	21	24
13	27	24
14	27	30
16	33	30
⋮	⋮	⋮

feasible combination.

Using a $N_s = 2p \pm 1$ combination results in an odd number of coils per phase which will limit the possibilities of series and parallel connections of the coils. It will also cause unbalanced axial forces between the rotors and the stator. All the $N_s = 2p \pm 2$ combinations give an even number of coils per phase. Hence, the coils can be connected both in series and in parallel configurations. The attracting forces between a rotor and the stator are in balance, since all coils consist of pairs which are displaced by 180 mechanical degrees.

3.4 Winding factors

The winding factor is defined as the distribution factor multiplied by the pitch factor which can be seen in (23).

$$k_{wn} = k_{dn} k_{pn} \tag{23}$$

Both the distribution factor and the pitch factor depend on the type of winding that is used. The following equations; (24)-(27) refer to *double-layer, non-overlap and slotted/segmented iron-cored windings* [5],

$$k_{dn} = \frac{sin(\frac{n\pi}{2m_1})}{zsin(\frac{n\pi}{2m_1 z})} \tag{24}$$

where n is the harmonic number, m_1 the number of phases and z the number of coils in a group. The number of coils in a group can be calculated as:

$$z = \frac{N_s}{m_1 F} \tag{25}$$

where F is the greatest common divisor (GCD) of the number of poles, $2p$, and the number of stator segments, N_s.

$$F = GCD(2p, N_s) \tag{26}$$

The pitch factor can be calculated according to (27),

$$k_{pn} = sin(\frac{n\pi p}{N_s}) = sin(\frac{\theta_{mn}}{2}) \tag{27}$$

where θ_{mn} corresponds to the coil span angle.

The winding factors for the feasible combinations of N_s/p up to 24/13 are shown in Table 3.

Table 3: Winding factors for the 1st to 13th harmonic for feasible pole pair and stator segment combinations up to $p = 13$ for a 3-phase YASA machine.

N_s/p	Harmonic number												
	1	**2**	**3**	**4**	**5**	**6**	**7**	**8**	**9**	**10**	**11**	**12**	**13**
6/2	0.866	0.866	0	-0.866	-0.866	0	0.866	0.866	0	-0.866	-0.866	0	0.866
6/4	0.866	-0.866	0	0.866	-0.866	0	0.8660	-0.866	0	0.866	-0.866	0	0.866
12/5	0.933	0.433	-0.500	-0.433	0.067	0	-0.067	0.433	0.500	-0.433	-0.933	0	0.933
12/7	0.933	-0.433	-0.500	0.433	0.067	0	-0.067	-0.433	0.500	0.433	-0.933	0	0.933
18/8	0.945	0.289	-0.577	-0.289	0.140	0	0.061	0.289	0	-0.289	-0.061	0	-0.140
18/10	0.945	-0.289	-0.577	0.289	0.140	0	0.061	-0.289	0	0.289	-0.061	0	-0.140
24/11	0.950	0.217	-0.604	-0.217	0.163	0	0.096	0.217	-0.104	-0.217	0.017	0	-0.017
24/13	0.950	-0.217	-0.604	0.217	0.163	0	0.096	-0.217	-0.104	0.217	0.017	0	-0.017

3.5 Torque calculations

More than one way of analytically calculating the torque production of an axial flux machine exist, previously presented in (6) and (7). As discussed by [6], the widespread acceptance for the Lorentz force method seems surprising, since it should be valid for a non-slotted machine but not for a slotted machine. In the slotted machine, the main part of the magnetic flux goes trough the stator core and not trough the conductors at all. A variation[2] of (7), which considers the product between the air gap areas, the magnetic loading and the electric loading, is used in this thesis:

$$T = \pi BQ \frac{D_o + D_i}{2} D_i \frac{D_o - D_i}{2} \tag{28}$$

where B is the magnetic loading and Q is the electric loading expressed as:

$$Q = k_{w1} \frac{2N_{ph} I_{ph}}{\pi D_i} \tag{29}$$

It was later verified that this torque expression gives a good correlation between the analytic and FEA results for this particular machine topology and size of geometry.

3.6 Magnetic flux and permanent magnet length

A very simple approach is to model the magnetic flux distribution as a square shaped distribution; see the dashed line in Figure 13, where the permanent magnets are assumed to cover 120 electrical degrees or 2/3 of the pole pitch. Using Fourier analysis, the peak value of the corresponding fundamental, $\hat{B}_1$, can be expressed as:

$$\hat{B}_1 = \frac{4\sqrt{3}}{2\pi} B_m \tag{30}$$

If the reluctances of the iron parts are neglected, the required length of the permanent magnets can be calculated as:

$$l_{pm} = \frac{\mu_{r,pm} l_g}{\frac{B_{r,pm}}{B_m} - 1} \tag{31}$$

where l_g is the axial length of the air gap, $\mu_{r,pm}$ is the relative permeability of the permanent magnets and $B_{r,pm}$ is the residual flux density of the permanent magnets.

[2]From discussions with Martin West at Volvo Technology in January 2011.

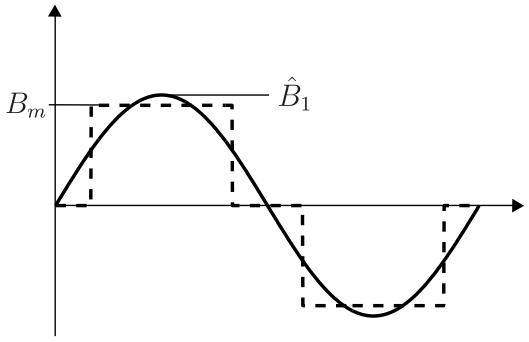

Figure 13: Air gap flux density.

As can be seen in Equation (31), in order to design a very compact machine with high magnetic loading, it is important to keep the air gap as small as possible; to minimize the air gap length itself and to minimize the length of the permanent magnets.

3.7 Rotor core length

If both the leakage flux and the induced flux are neglected, the total air gap flux per pole can be calculated as the product of the flux density and the area of a permanent magnet:

$$\phi_g = B_{pm} A_{pm} = \frac{2}{3} B_m \pi \frac{R_o^2 - R_i^2}{2p} \tag{32}$$

where a magnet is assumed to cover 2/3 of a pole area. As illustrated in Figure 14, the magnetic flux density in the θ-direction trough the rotor back can be expressed as:

$$\phi_r = A_r B_r = l_r (R_o - R_i) B_r \tag{33}$$

where B_r is the magnetic flux density in the rotor back.

Hence $2\phi_r = \phi_g$, as half of the flux per pole goes trough the rotor back in the θ-direction and the other half in the $-\theta$-direction, which can be seen in Figure 6d. The required rotor core length can be calculated as:

$$l_r = \frac{B_m}{B_r} \frac{\pi}{6p} (R_i + R_o) \tag{34}$$

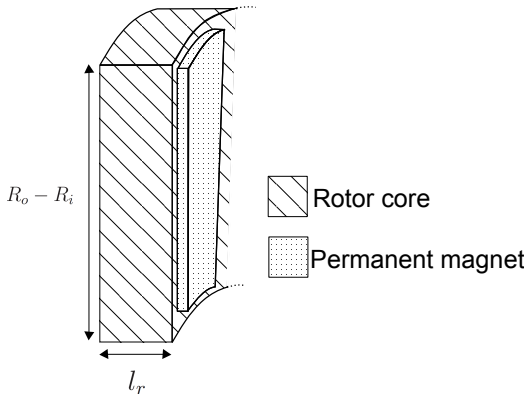

Figure 14: Schematic figure of the cross-sectional area, A_r, of the rotor back.

3.8 Stator segment

A schematic figure of a stator segment is shown in Figure 15. It can be divided into three parts: two shoes and one central bar. The shoes are wider in both the radial- and the θ-direction to overlap the windings and maximize the active surface. This results in a three dimensional flux path (axial-, radial- and θ-direction), therefore the shoes can not be made of laminated steel. In the central bar, on the other hand, the flux path is only in the axial direction and it is possible to use laminated steel or soft magnetic composite (SMC). SMC has lower permeability but also lower losses at higher frequencies compared to those of laminations. Hence, the choice of material for the central bar can be motivated by the electric frequency. However, using two different materials will add extra complexity due to the non-ideal contact surfaces. Entire SMC stator segments are therefore considered.

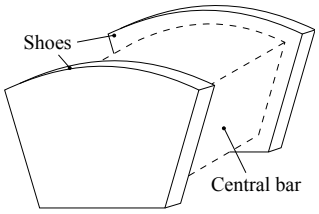

Figure 15: Schematic figure of a stator segment.

The cross-sectional area of the central bar, A_s illustrated in Figure 16, required for the desired magnetic flux density, B_s, can be expressed as:

$$A_s = \frac{\phi_s}{B_s} = \frac{2}{3}\frac{B_m}{B_s}\pi\frac{R_o^2 - R_i^2}{2p} \tag{35}$$

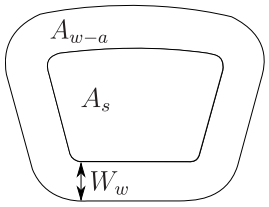

Figure 16: Schematic figure of the central bar and the winding behind the stator segment shoe.

The relation between the width of the copper winding, W_w, around the central bar and the area of the winding, A_{w-a}, seen in the axial direction in Figure 16 can be approximated as:

$$A_{w-a} = \left(2(R_o - R_i) + (\frac{\pi D_o}{2p} - 2W_w) + (\frac{\pi D_i}{2p} - 2W_w)\right)W_w \qquad (36)$$

Finally, the cross-sectional area of the central bar, A_s, and the area of the winding, A_{w-a}, must be chosen to fit into the area that is available for each stator segment:

$$A_{statorsegment} = \frac{air\ gap\ area}{N_s} = \frac{\pi(R_o^2 - R_i^2)}{N_s} = A_s + A_{w-a} \qquad (37)$$

3.9 Inductances

A very simplified way of calculating the inductance per phase is to transform the machine geometry to a an equivalent C-core, see Figure 17. The inductance of a C-core can easily be approximated if the flux leakage and the fringing effects are neglected, i.e. $l_{g-C} \ll A_{g-C}$, and if also the permeability is assumed to be much greater inside the core than in the air gap. The approximated inductance is then:

$$L = \frac{\mu_0 n^2 A_{g-C}}{l_{g-C}} \qquad (38)$$

which is shown by [16] for example.

When the number of stator segments is chosen as $N_s = 2p \pm 2$ according to section 3.3, the number of stator segments per phase is always an even number. As mentioned previously, the stator segments in each phase can then be divided into pairs, displaced 180°mech. The coils around those pairs should be connected in series to make sure that the attracting forces between the rotors and the stator are balanced (two axial forces of the same magnitude

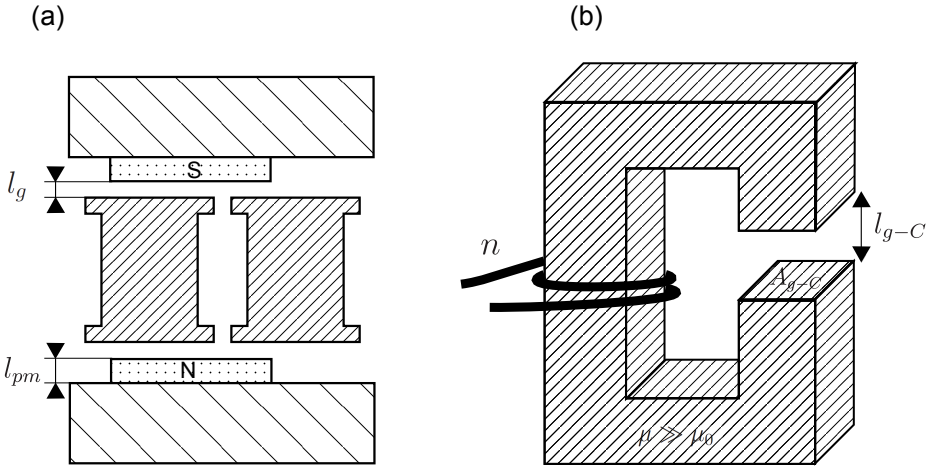

Figure 17: C-core transformation to calculate the inductance.

displaced 180°mech.). To further simplify the situation, all coils are assumed to be connected in series.

A stator segment pair is shown in Figure 17a, drawn side by side to reduce the figure. The corresponding l_{g-C} can be calculated as:

$$l_{g-C} = 4(l_{pm} + l_g) \tag{39}$$

and the corresponding air gap area, A_{g-C}, can be approximated as:

$$A_{g-C} = \frac{\pi R_o^2}{N_s} - R_i^2 tan(\frac{\pi}{N_s}) \tag{40}$$

which is the area of the stator segment shoe that faces the air gap.
The fact that a three phase machine is considered together with (38)-(40) gives the expression for the phase inductance:

$$L_s = \frac{\mu_0(\pi R_0^2 - N_s R_i^2 tan(\frac{\pi}{N_s}))n^2}{6(l_g + l_{pm})} \tag{41}$$

where n is the number of turns around each stator segment.

3.10 Losses and efficiency

The electromagnetic losses in the machine can be subdivided into copper and iron losses. In this project, the copper and the iron losses are calculated in the FEA part. The iron losses are calculated in the time domain according to the method suggested by [17]. This should give a more accurate prediction of the hysteresis losses than the classic method that is calculated in the frequency domain. The classic analytic methods are briefly described in this section to explain the mechanisms that cause the losses.

3.10.1 Copper losses

The winding resistance for direct current can be calculated using (42):

$$R_{s-DC} = \frac{n \cdot l_{av}}{a_p \cdot A \cdot \sigma_{cu}} \tag{42}$$

where n is the number of turns, a_p is the number of parallel conductors within each turn, l_{av} is the average length of a turn, A is the cross-sectional area of the conductor and σ_{cu} is the conductivity of copper. A constant, K, can be introduced to compensate for the temperature and the content of harmonics in the current:

$$P_{cu} = m_1 \cdot i_s^2 \cdot R_s = m_1 \cdot i_s^2 \cdot K \cdot R_{s-DC} \tag{43}$$

where m_1 represents the number of phases. Various analytical methods that considers temperature dependence and the skin effect due to the harmonics were investigated in [5] and [18].

Eddy currents are induced in the conductors since these are exposed to an alternating magnetic field in the air gap. This can generally be ignored for slotted AFPM but should be considered for slotless AFPM [5].

3.10.2 Iron losses

Accurate computation of the iron or core losses is a complicated task. The iron losses are subdivided into three parts [18]:

- Hysteresis losses
- Eddy current losses
- Excess losses

The hysteresis losses are caused by the energy needed to flip the magnetic dipoles within the soft magnetic material [16]. Material with high permeability and low coercivity should be chosen to minimize the hysteresis losses.

Eddy currents are induced in the iron parts due to the alternating magnetic flux from the stator windings and the field from the rotating permanent magnets. The induced currents can be limited by lamination of the core. The core is therefore constructed of thin sheets separated by a material with lower conductivity. The eddy current losses increase with frequency, which is related to the current harmonics and the speed. A few simple methods of predicting the losses per unit volume are shown by [18]. An example can be seen in (44),

$$P_{Fe} = k_{hys}\hat{B}^2 f + \pi^2 \frac{\sigma_{Fe} d^2}{6}(\hat{B}f)^2 + 8.67 \cdot k_{ex}(\hat{B}f)^{1.5} \tag{44}$$

where k_{hys} is the hysteresis loss coefficient, k_{ex} is the excess loss coefficient, d is the thickness of the steel sheets and σ_{Fe} is the electric conductivity of the ferromagnetic material. The loss coefficients can be determined from loss curves as a function of frequency, which may be provided by the manufacturers.

3.10.3 Efficiency

The efficiency of the electric machine is defined as:

$$\eta = \frac{P_{out}}{P_{in}} = \frac{P_{out}}{P_{out} + P_d} \tag{45}$$

where P_{out} is the mechanical output power, P_{in} is the electrical input power and P_d is the total power losses in the machine.

4 Analytic design

The intention of this section is to describe the analytic part of the design process. As explained before, this is not a complete analytic design procedure as the analytic design and FEA are made alternately in this thesis. Therefore, values from the FEA, in section 5, are sometimes used as input to the analytic design part in this section.

4.1 Number of pole pairs and stator segments

The number of pole pairs, p, should be chosen considering several aspects. High pole numbers give:

- Smoother torque
- Higher winding factor/torque
- Better magnetic balance
- Possible reduction of the amount of iron for the same magnetic loading, shown in (34) and (35). The electric loading and the torque may then be increased.

On the other hand the pole pair number is limited by:

- Increased switching frequency and switching losses
- Increased iron losses
- Flux leakage
- Practical/mechanical aspects (constructions comprised by many small parts)

The mechanical system is schematically visualized in Figure 18. The fundamental of the electric frequency, f_{el}, at a given vehicle speed can be calculated using (46).

$$f_{el} = \frac{\omega_w}{2\pi} \cdot g_R \cdot p \tag{46}$$

where ω_w is the angular frequency of the wheel, g_R is the gear ratio of the planetary gear and p is the pole pair number. Using the wheel radius of 0.492 m together with (46), the electric frequency as function of vehicle speed is plotted in Figure 19 for four different gear ratios and four different pole

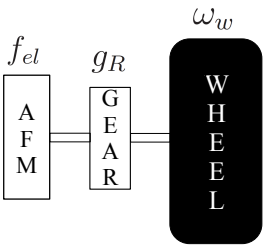

Figure 18: Schematic figure of the mechanical system.

pair and stator segment configurations.

During this work it was indicated, by people working with the planetary gear, that a one-stage gear ratio is limited to 6-7. The loss cross over frequency is assumed to be around 1kHz, as the losses for laminated core materials increase faster than the losses for SMC materials with respect to the electric frequency. It can then be seen in Figure 19 that use of SMC cannot be motivated for reduction of the iron losses for any combination.

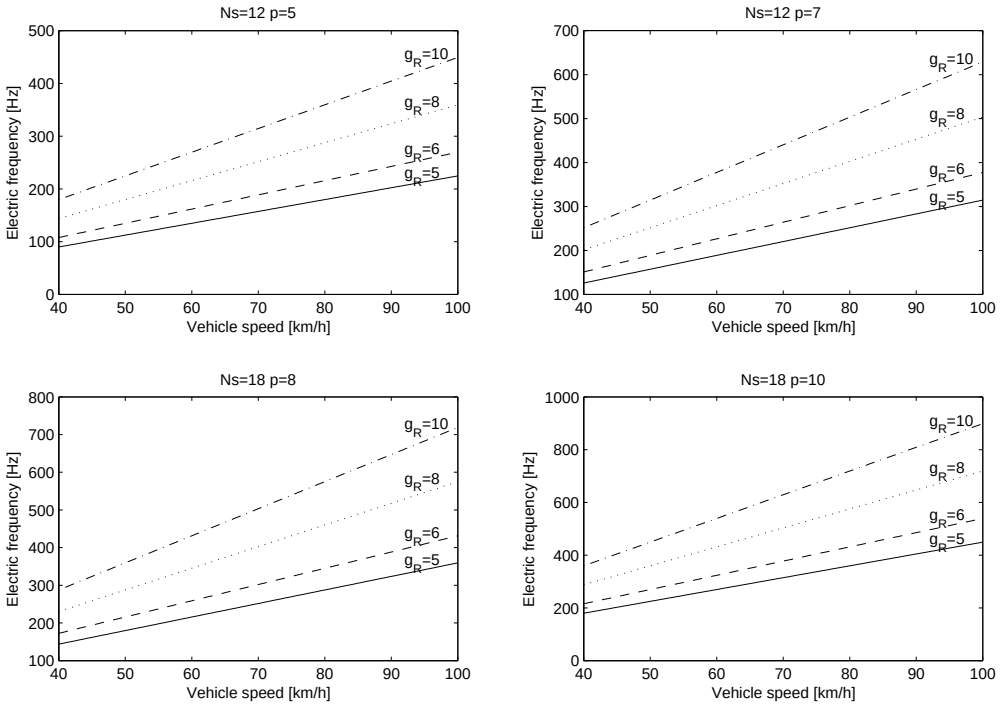

Figure 19: Electric frequency for four different gear ratios (5, 6, 8, 10) and possible combinations of pole pairs and stator segments.

As described in section 3.3, the number of stator segments is directly influenced by the number of poles. A $N_s = 2p \pm 2$ configuration is preferable due to its balanced characteristics, the possible choices are previously shown in Table 2.

The outer width, W_o, and the inner width, W_i of a permanent magnet and a stator segment shoe according to Figure 20 can be calculated using (47) and (48).

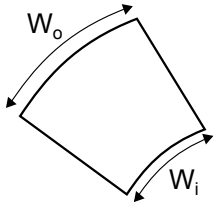

Figure 20: Outer and inner width of a permanent magnet or a stator segment shoe.

$$W_{s-segment} = \frac{\pi D}{N_s} \tag{47}$$

where D is the diameter and N_s is the number of stator segments.

$$W_{pm} = \frac{\pi D}{p} \frac{120}{360} \tag{48}$$

where p is the number of pole pairs and a magnet is assumed to cover 120 electrical degrees.

The resulting widths, W_o and W_i, for six different N_s/p combinations are calculated and presented in Table 4. Some extra space between the stator segments is of course needed in order to prevent flux leakage between the segments.

Two examples of YASA machine designs are presented in [2] and [9]. An N_s/p configuration of 12/5 is used in both cases. Their geometries are slightly smaller but in the same order of magnitude (machine diameters of 186 mm and 204 mm compared to 260 mm). The N_s/p=12/5 configuration is used as a starting point for this design. The lower numbers give very unfavorable winding factors.

Table 4: Magnet and stator segment widths for different N_s/p combinations.

	Magnet width [mm]		Stator segment width [mm]	
$\mathbf{N_s/p}$	$\mathbf{W_i}$	$\mathbf{W_o}$	$\mathbf{W_i}$	$\mathbf{W_o}$
12/5	34.9	54.5	43.6	68.0
12/7	25.0	38.9	43.6	68.0
18/8	21.8	34.0	29.0	45.4
18/10	17.4	27.2	29.0	45.4
24/11	15.8	24.8	21.8	34.0
24/13	13.4	21.0	21.8	34.0

4.1.1 Winding configuration and inductance

Using the coil span angle in (27), the phase displacement of the induced fundamental back-EMF in the coils can be expressed as:

$$\theta_{emf-coil} = n_{coil} \cdot \frac{2\pi p}{N_s} \tag{49}$$

where n_{coil} represents the index of the coil.

The phase orientation of the fundamental of the induced back-EMF in the twelve coils is plotted in Figure 21. It can be seen that the two coils that form a pair, displaced 180 mechanical degrees, also are shifted 180 electrical degrees. As mentioned in section 3.3, the pairs should be connected in series to make sure that the axial forces are balanced. The windings are arranged in phase groups that consist of coils with the smallest possible phase displacement in between. They are connected in series, the circuit diagram is shown in Figure 22

The phase inductance that is calculated according to (41) becomes $1.47\mu\text{H}/n^2$.

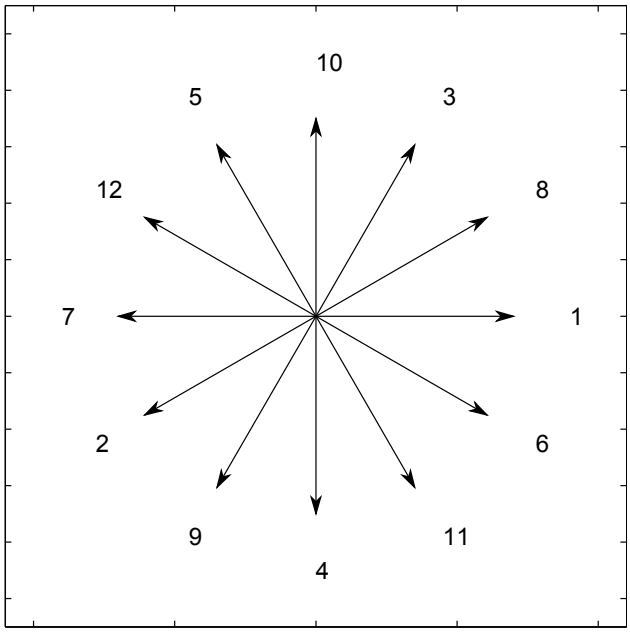

Figure 21: Induced back-EMF phase displacement between the coils.

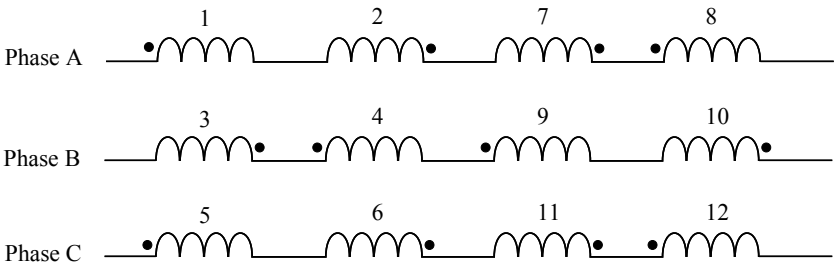

Figure 22: Circuit diagram of the winding configuration.

4.2 Optimization of the geometry for maximal torque

As mentioned previously, the theoretic ratio between outer and inner diameter for maximum torque is given by $\lambda = \frac{1}{\sqrt{3}} = 0.58$. Optimal ratios for different topologies and machine sizes are suggested by [2], [7], [9], [10] and [19]. The highest torque density can be reached for ratios between 0.6 and 0.7 according to one approach in [7]. For the YASA machine designs in [2] and [9], ratios of 0.58 and 0.65 are used respectively. A ratio of 0.64, which is included in the range above, is therefore assumed for the design in this thesis.

The product of magnetic and electric loading should be maximized in order to obtain the highest possible torque according to (28). The idea is to match the copper and iron quantities to get a high utilization of both materials, thereby avoiding a bottleneck situation when one of them is saturated too long before the other one is fully utilized.

A maximum flux density of 1.7 T and a maximum current density of 7 A/mm^2 rms are assumed to be reasonable values for high utilization of the materials. The magnetic flux density is chosen to stay within the saturation limit of the iron, which is about 2 T. The current density has been chosen based on values for existing machines, but may be a bit conservative when comparing with the YASA machine design in [9]. The air gap length is kept constant at 1 mm, which is assumed to be a practical length to give mechanical clearance. The axial length of the stator segment shoe is assumed to be 5 mm, while all the other geometric variables are varied in order to find the maximal torque within the given volume.

The peak flux density of the fundamental in the air gap, $\hat{B}_1$ in (30), is used as an input to an optimization script. The value of $\hat{B}_1$ together with the assumed maximum flux density of 1.7 T in the iron are then used to determine the geometry of the magnetic circuit according to previously presented relations.

The space that is left (A_{w-a} in Figure 16 together with the length of the central bar) when the geometry of the stator segments is determined, corresponds to the total cross-sectional area of the winding, A_w. This area is filled with copper using an assumed fill factor of 70%; copper fill factors up to 78% for pre-pressed windings in segmented fractional slot machines are reported according to [20].

$$K_{cu-fill} = \frac{A_{cu}}{A_w} \tag{50}$$

The electric loading can be calculated using the copper area, A_{cu} in (50), together with the assumed maximum current density of 7 A/mm^2. The resulting torque is calculated based on magnetic loading and electric loading using (28).

Lower values of magnetic loading give a rotor back thickness that is too small to make sense. If the calculated rotor back thickness is below 9.5 mm it is simply forced to 9.5 mm which is assumed to be a reasonable starting value.

The magnetic and electric loading for different geometries is shown in Figure 23 when varying the air gap flux density while the core magnetic flux end current densities are kept constant.

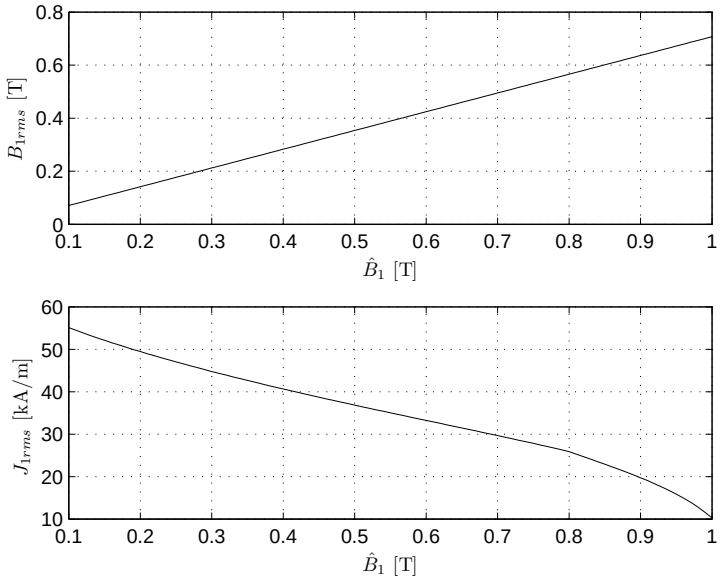

Figure 23: Magnetic and electric loading when the geometry is changed to keep the current density in the copper and magnetic flux density in the iron constant while the air gap flux density, $\hat{B}_1$, is varied.

The analytically calculated torque is presented in Figure 24, where the lower torque for low values of $\hat{B}_1$ corresponds to geometries that give a mismatch between electric and magnetic loading in favor of the electric loading. The maximum for the analytically calculated torque is received for $\hat{B}_1 \approx 0.75$ T.

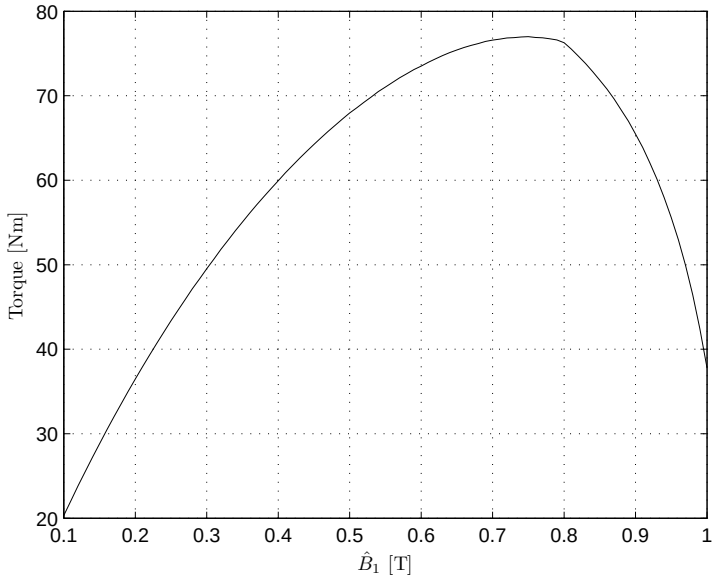

Figure 24: Analytically calculated torque when the geometry is changed to keep the current density in the copper and magnetic flux density in the iron constant while the air gap flux density, $\hat{B}_1$, is varied.

4.3 Investigation of torque speed characteristics

This subsection describes how the machine torque speed characteristics can be changed based on the number of turns for a given maximum voltage. All quantities needed in order to find the torque speed characteristics according to section 3 are expressed as functions of the number of turns, n. The machine geometry (the geometry that corresponds to $\hat{B}_1$=0.85 T in section 5.2) is fixed as it has been optimized to give the maximum torque for the assumed current and flux densities of 7 A/mm^2 and 1.7 T.

The maximum phase peak voltage is calculated to 273 V according to (20), where an amplitude modulation ratio, m_a, of 95% is used to stay within the linear region of the inverter with reasonable margin.

The total current in a winding around a stator segment can be calculated as:

$$I_{tot-winding} = J_{cu} \cdot A_{cu} = J_{cu} \cdot A_w \cdot K_{cu-fill} \tag{51}$$

where J_{cu} is the current density in the conductors (7 A/mm^2), A_{cu} is the total conductor cross-section area and A_w is the cross-section area of the winding.

The maximum phase peak current is then:

$$\hat{I}_{ph-max} = \frac{\sqrt{2}}{n} I_{tot-winding} \tag{52}$$

Hence, with the current density fixed:

$$\hat{I}_{ph-max} \sim \frac{1}{n} \tag{53}$$

The relation between the phase flux linkage due to the permanent magnets (open circuit) and the number of turns around each segment is:

$$\psi_m \sim n \tag{54}$$

Considering the C-core analogy in section 3.9, the relation between the inductance and the number of turns is:

$$L \sim n^2 \tag{55}$$

The relation between phase resistance and number of turns is:

$$R \sim n^2 \tag{56}$$

which may cause confusion but both the cross-sectional area of the conductor and the total length of the conductor in each coil are affected by the number of turns, see (42). This to keep the current density, J_{cu}, the total current, $I_{tot-winding}$, and the geometry constant while the number of turns are varied.

Values from the FEA part in section 5 are used to analytically calculate the torque speed characteristics of the machine. The values are summarized in Table 5.

Table 5: Values that are determined in the FEA and used for analytic calculations of torque speed characteristics.

$\hat{U}_{ph-1}$	273.13 V
$I_{tot-winding}$	1.60 kA
ψ_m	0.0054 Wb/n
L_d	2.56 $\mu H/n^2$
L_q	2.14 $\mu H/n^2$
R	45.9 $\mu\Omega/n^2$

In Figure 25, the torque as a function of speed is plotted for n=20,n=30,n=40 and n=50. As expected, the constant torque region is decreased for higher number of turns and the slope of the torque becomes steeper in the constant power region.

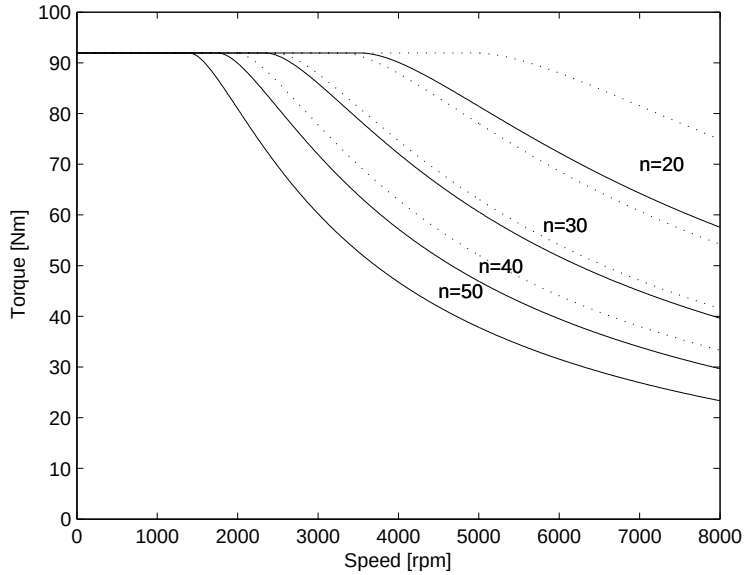

Figure 25: Torque as function of speed for n=20,n=30,n=40 and n=50. The dotted lines show the characteristics for a DC-link voltage of 700 V instead of 500 V.

In Figure 26, the output power as function of speed is shown for the four variations of n. A machine with a lower number of turns is able to produce more output power, since it enters its field weakening region at a higher speed compared to a machine with higher a number of turns.

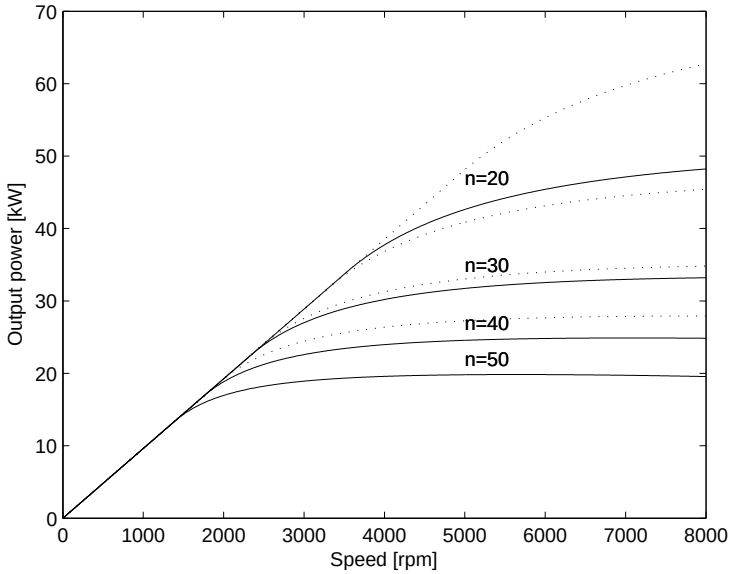

Figure 26: Output power as function of speed for n=20,n=30,n=40 and n=50. The dotted lines show the characteristics for a DC-link voltage of 700 V instead of 500 V.

The corresponding power factors are plotted as function of speed in Figure 27. One can see that greater field weakening performance and output power production are received at the cost of a poor power factor.

Below base speed, the power factor is approximately 0.75. This indicates that the machine geometry is close to a theoretical infinite speed machine, which has a theoretic maximum power factor of $\frac{1}{\sqrt{2}} = 0.71$ in the constant torque region. This implies that the value of $\frac{\psi_m}{L}$ is close to the maximum current, i, according to the theory in section 3.

One can also observe the equal power factors in their constant torque region, explained by the fact that both $\frac{\psi_m}{L}$ and i are inversely proportional to the number of turns, n. Therefore, the center of the voltage limit circles in relation to the current limit circle, seen in Figure 10, cannot be moved by changing the number of turns, they are scaled together.

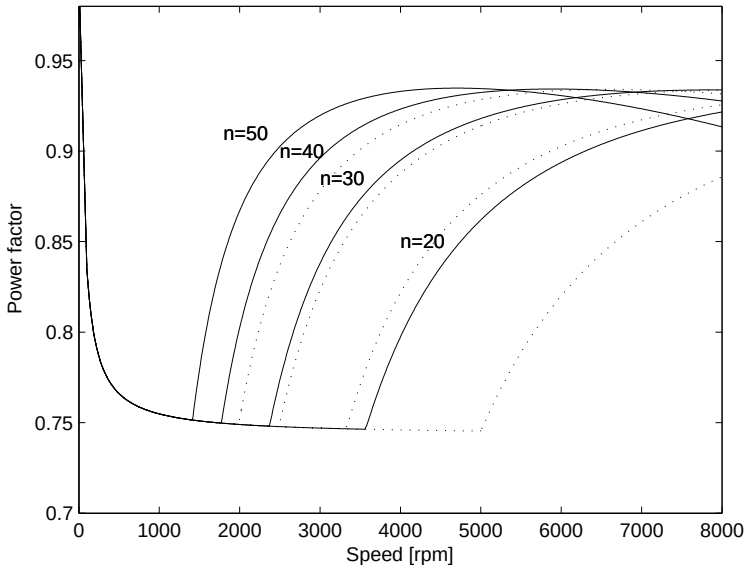

Figure 27: Power factor as function of speed for n=20,n=30,n=40 and n=50. The dotted lines show the characteristics for a DC-link voltage of 700 V instead of 500 V.

The nominal phase currents for the different selections of the number of turns are summarized in Table 6. In section 5.4 the inductances in positive and negative d- and q-direction are calculated per number of turns in square. The phase inductance is plotted as a function of the number of turns in Figure 28.

Table 6: Nominal phase rms current for n=20,n=30,n=40 and n=50.

Number of turns	**Nominal phase rms current [A]**
20	80.2
30	53.5
40	40.1
50	32.1

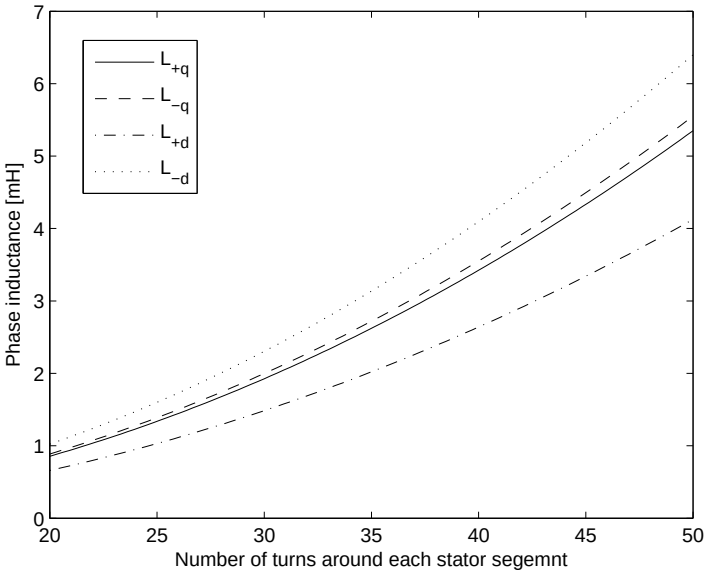

Figure 28: Phase inductance at 7 A/mm^2 as a function of the number of turns around each stator segment, n.

As no requirements in terms of rated speed, rated torque etc. were stated for the machine, the choice of the number of turns is based on an indicated maximal speed of around 3000 rpm. When comparing n=20 and n=30, the output power and the torque at 3000 rpm can be increased by 6.7% (with n=20) at the cost of a 50% higher current. The inductance is about two times higher for n=30 compared to n=20 according to Figure 28. The current ripple is thereby two times lower using the same switching frequency and DC-link voltage. Hence, the ripple is lower for n=30 also in relation to the amplitude of the fundamental of the current. Therefore n=30 is chosen, this results in a nominal current of 53.5 A and a nominal speed of around 2400 rpm.

5 Finite element analysis

The finite element analysis is made in Ansoft Maxwell 3D version 14, therefore some terminology from this software is used in the report.

5.1 Model and implementation

5.1.1 Symmetry planes

The model of the whole machine is shown in Figure 29a. Two symmetry planes exist in the geometry, the xy-plane and the xz-plane.

The machine is first split and reduced along the xy-plane using an "Even (flux normal)" symmetry boundary. This boundary condition is also called Neumann's condition and forces the flux lines to be normal to the symmetry surface, see Figure 29b. It is equivalent to having an external material with infinite permeability just outside the surface [21].

The geometry is then split along the xz-plane and further reduced using "Master" and "Slave" boundaries, which is also called periodic boundary condition and can be seen in Figure 29c. It is split in two parts since 2 is the greatest common divisor of $N_s = 12$ and $2p = 10$. The computational domain is now reduced to a quarter of the initial machine.

In Maxwell 3D, most of the machine properties can be calculated using the quarter machine while at least the half machine has to be used for some properties. The model of the whole machine has been used to verify the results from the reduced models for a limited number of simulations.

5.1.2 Windings

The windings or the coils are modeled as solid objects to simplify the geometry. A coil terminal is introduced as a surface, the cross-sectional area of the solid winding, of which the normal is in the current direction. As the real coils consist of several turns of a conductor, each turn carrying the same current, the current density is expected to be more or less evenly distributed. The windings are therefore modeled as "Stranded" conductors, which forces the current to be evenly distributed in the solid object.

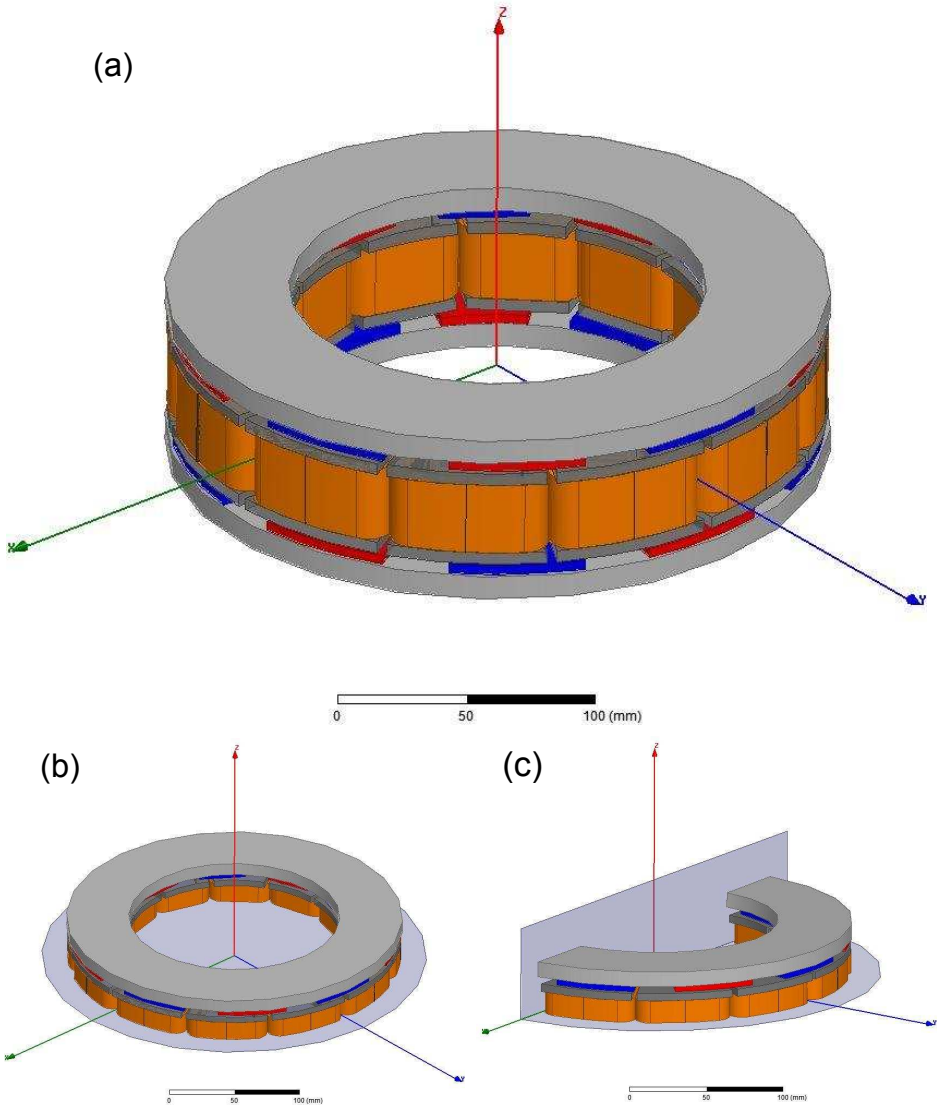

Figure 29: Reduction of the 3D-model using symmetry planes.

5.1.3 Core material

Höganäs AB[3] kindly supplied data of suitable SMC materials. Four materials were suggested for the application and their BH-curves can be seen in Figure 30. Somaloy 1000 3P was chosen due to its preferable BH-characteristics for high magnetic flux densities. Its loss characteristics, shown in Figure 31, were slightly less favorable than the other materials' (not shown here) but thanks to its BH-characteristic, it was regarded as suitable for maximizing

[3]http://www.hoganas.com/

the torque and power densities of the machine.

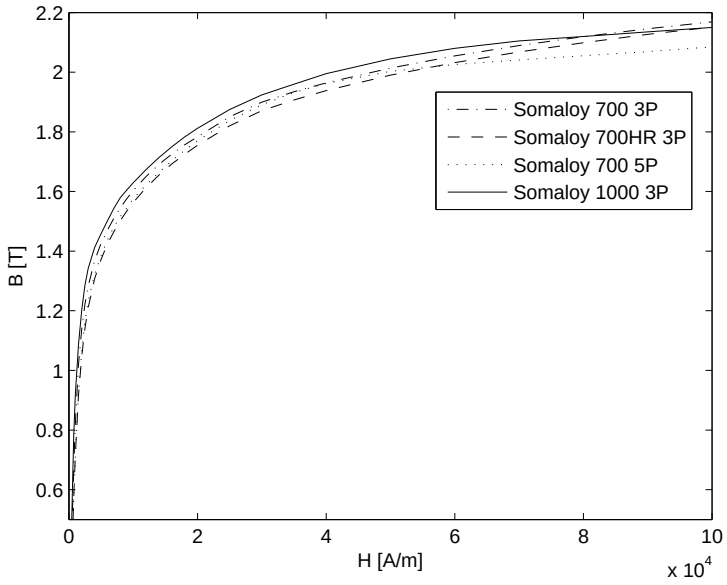

Figure 30: Four different SMC materials suggested by Höganäs (Source: Höganäs "Data adjusted for use in Finite Element modeling").

The BH-curve for Somaloy 1000 3P in Figure 30 together with its loss characteristics, shown in Figure 31, are extrapolated and used to simulate the non-linear behavior of the SMC material in Maxwell 3D. The SMC material is used both in the stator segments and in the rotor cores.

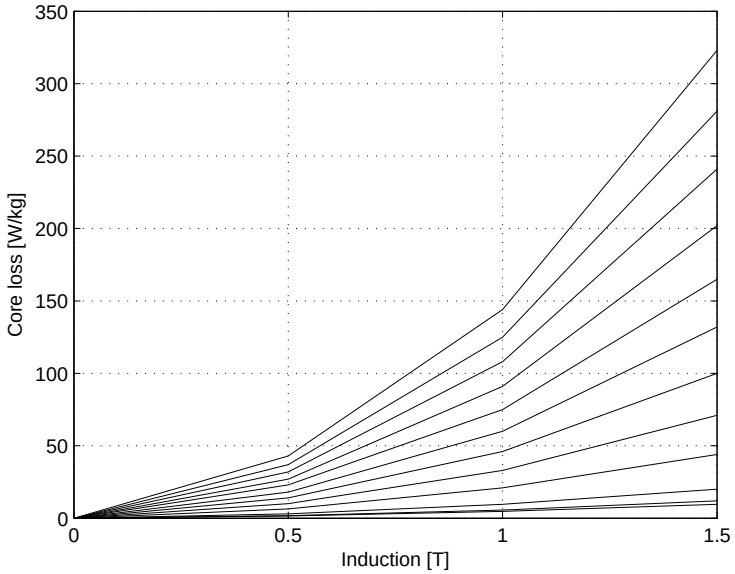

Figure 31: Core loss for Somaloy 1000 3P, from bottom: f=50, 60, 100, 200, 300, 400, 500, 600, 700, 800, 900 and 1000 Hz (Source: Höganäs "Datasheet of Somaloy 1000 3P (0.3% 3P Lube), 800 MPa").

5.1.4 Permanent magnets

Sintered Neodymium-Iron-Boron (NdFeB) magnets called N35EH were chosen to model the permanent magnets. They offer high magnetic output at a reasonable cost, and were recently used in another machine design by Volvo Technology. A simple linear model is used in the FEA-model, where data from [22] is used.

The properties of the permanent magnets change significantly depending on temperature. A temperature of 120°C has been assumed, which yields a relative permeability, $\mu_{r,pm}$, of 1.04 and a coercivity, H_c, of 795.57 kA/m according to the datasheet.

If the temperature is assumed too low, there is a risk that the magnetic loading and thereby the torque is overestimated. On the other hand, if it is assumed too high, there is a risk that the required amount of iron is underestimated.

5.1.5 Losses

Copper

As the coil terminal is modeled as a surface that covers the whole cross-sectional area of the winding, the conductivity for the winding object is scaled using the copper fill factor:

$$\sigma_w = \sigma_{cu} \cdot K_{cu-fill} \tag{57}$$

The conductivity in (57) together with the total current in (51) are used to get the correct resistive copper losses when stranded conductors are used in 3D. The average length of a turn is determined by the geometry of the winding object, which gives the DC-resistance according to (42). Thereby the expected frequency dependence of the copper losses is not taken into account in this model.

Iron

Core losses are often calculated in the frequency domain, as shown in section 3.10.2. A dynamic model, in time domain, using the time derivatives of the flux density together with loss data for the material is used to calculate the core losses in Maxwell 3D [4]. In this way, both the frequency and the magnetic flux density dependences together with the non-linear BH-curve are taken into account in the model.

5.2 Optimization of the geometry for maximal torque

The same procedure as in section 4.2 was carried out in the FEA part to find the geometry that gives the maximum torque. The torque for five FEA variations can be seen in Figure 32, together with the previous analytically calculated torque. As can be seen, higher magnetic loading which is achieved at the cost of electric loading is required in order to obtain the maximal torque.

The difference can be explained as a consequence of the simplifications made to analytically calculate the magnetic loading. The permeability of the iron was set at infinity and the leakage was neglected. The magnetic loading is thereby overestimated.

[4] Accordning to "Maxwell 3D user's guide", provided by Ansoft.

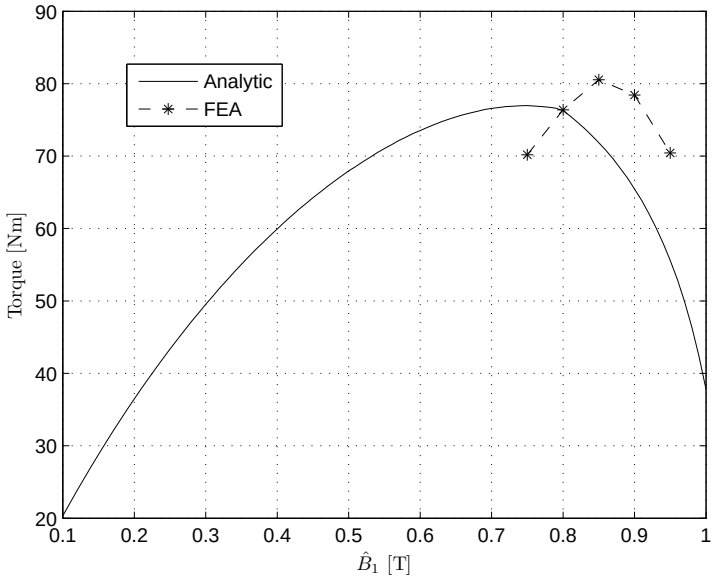

Figure 32: Torque from FEA and analytic calculations when the geometry is changed to keep the current density in the copper and magnetic flux density in the iron constant while the air gap flux density, $\hat{B}_1$, is varied.

As the idea was to keep the maximum magnetic flux density in the iron parts constant (1.7 T) while the geometry was varied, the peak values of the flux densities in the middle of the stator segments were measured in the FEA model. The flux densities at open circuit tests are plotted as a dashed line in Figure 33, where the magnetic flux density is about 1.4 T which is below the target. Again, this is a consequence of the simplifications that were made in the analytic models. It can also be seen that it is almost constant for the two lowest values of $\hat{B}_1$ while it starts to increase for higher values of $\hat{B}_1$. This may be caused by the model used to calculate the required length of the permanent magnets, (31), which approaches infinity when B_m=B_{r-pm}. It is then probable that the required length of the permanent magnets is overestimated for the higher values of magnetic flux density.

In Figure 33, the flux density is also plotted when the machine is fed with rated current. As can be seen in the figure, the induced flux has a significant impact on the magnitude of the total flux. Actually, it is the total flux that is of interest when the utilization of the iron is evaluated. Ideally, the geometry for constant flux density of the total flux should therefore be found

iteratively. This was not possible due to the restricted time for this master thesis, where the geometry for $\hat{B}_1$=0.85 T is considered as the optimum design, as it gives the maximum torque according to Figure 32 and a flux density close to 1.7 T according to Figure 33.

One could discuss if the amount of iron should be reduced a bit for the geometries where $\hat{B}_1$ >0.85 T, as they are not "fully utilized" to 1.7 T. The electric loading could then be slightly increased and the maximum of the obtained torque in Figure 32 further moved towards higher values of $\hat{B}_1$.

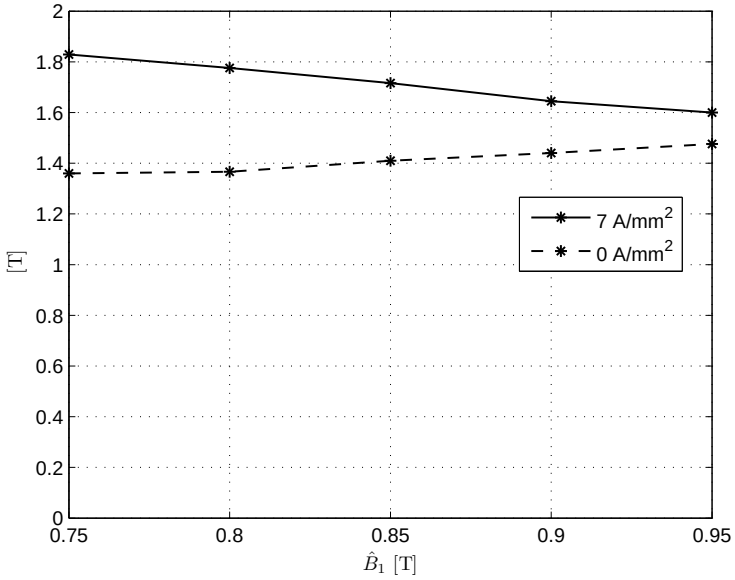

Figure 33: The flux density in the middle of the central bar when the geometry is changed to keep the current density in the copper and magnetic flux density in the iron constant while the air gap flux density, $\hat{B}_1$, is varied.

Figure 34 shows the analytically calculated geometric variations that are used in the FEA model, in the optimization procedure.

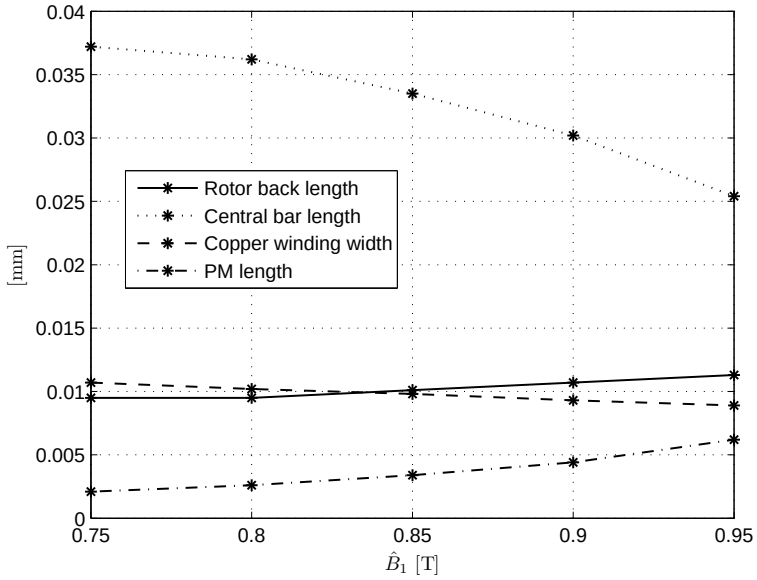

Figure 34: Geometric variables that are used for keeping the current density in the copper and magnetic flux density in the iron constant while the air gap flux density, $\hat{B}_1$, is varied.

5.2.1 Output power, losses and efficiency at 3000 rpm

Transient[5] simulations considering a steady state operation point at 3000 rpm were carried out for the five variations to compare their characteristics in terms of output power, losses and efficiency. Output power can be seen in Figure 35, and it is increased by approximately 15% when comparing the lowest and highest values that are obtained.

As described in section 5.1.5, the losses are subdivided into copper losses and iron losses, as shown in Figure 36. The copper losses decrease with decreased electric loading as expected. As shown in Figure 33, the induced magnetic flux contributes significantly to the total magnetic flux. The iron losses are therefore reduced even though the magnetic loading and the iron volume are increased, see Figure 36.

When efficiency, copper losses and iron losses are taken into account, it is shown that an optimization with respect to torque does not give an optimization of the efficiency, see Figure 37. It may also indicate that the geometry

[5]Time stepping simulations are made in transient simulation mode in Maxwell 3D.

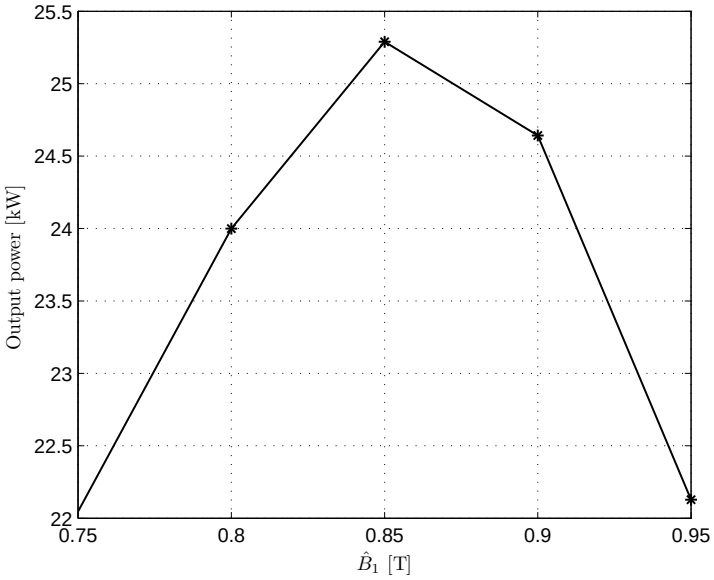

Figure 35: The output power at 3000 rpm for the five variations of the geometry.

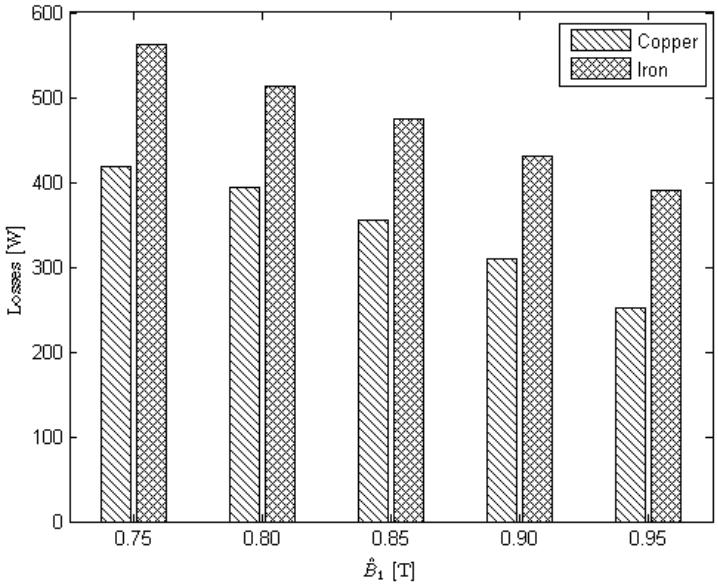

Figure 36: The losses at 3000 rpm for the five variations of the geometry.

should be chosen in favor of magnetic loading if efficiency is the optimization target, when current and flux densities of 7 A/mm^2 and 1.7 T are used.

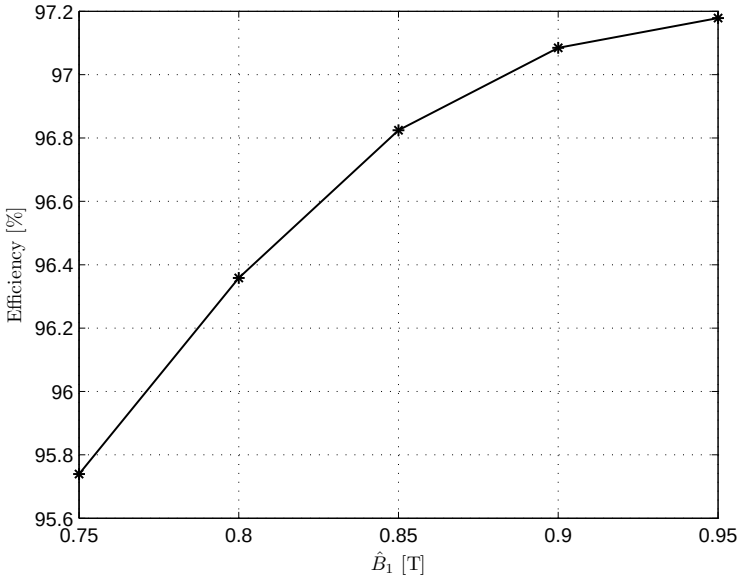

Figure 37: The efficiency at 3000 rpm for the five variations of the geometry.

5.2.2 Final geometry

The geometry corresponding to $\hat{B}_1$=0.85 T which gives the maximum torque is chosen as the final geometry. It has been determined by: the initial requirements, some assumptions and the torque optimization procedure (FEA) previously described. Table 7 presents the variables and how they were established.

Table 7: Variable summary for the machine design.

Variable	Description	Value	Requirement	Assumption	Calculations
D_o	Outer diameter	260 mm	×		
λ	Diameter ratio	0.64		×	
D_i	Inner diameter	166.4 mm			×
l_{tot}	Machine length	72.5 mm	×		
p	Number of pole pairs	5		×	
N_s	Number of stator segments	12		×	
$l_{air-gap}$	Air gap length	1 mm		×	
l_{shoe}	Stator shoe length	5 mm		×	
$l_{shoe-space}$	Stator shoe space	4 mm		×	
l_{pm}	Permanent magnet length	3.4 mm			×
l_r	Rotor core length	10.1 mm			×
$l_{central-bar}$	Stator segment central bar	33.5 mm			×
W_w	Width of copper winding	9.8 mm			×

5.3 Flux linkage and back-EMF

The flux linkage and back-EMF wave forms of the machine are calculated without current excitation at 3000 rpm and with one turn around each stator segment, $n = 1$.

Figure 38 shows the flux linkage of the three phases. As can be seen in the figure, they are sinusoidal with low harmonic content. This is also confirmed by the FFT of the flux linkage in Figure 39, where the amplitudes of all the higher harmonics that are shown are less than 0.5% of the fundamental. The fundamental of the flux linkage, ψ_m, is determined to 5.36 mWb/n.

The back-EMF wave forms for the three phases are displayed in Figure 40. As can be expected, their wave forms show a higher harmonic content than the flux linkage wave forms shown previously. Again, this is confirmed by the FFT of the back-EMF which is shown in Figure 41. The 11th harmonic, which has the greatest amplitude of the harmonics that are shown in the

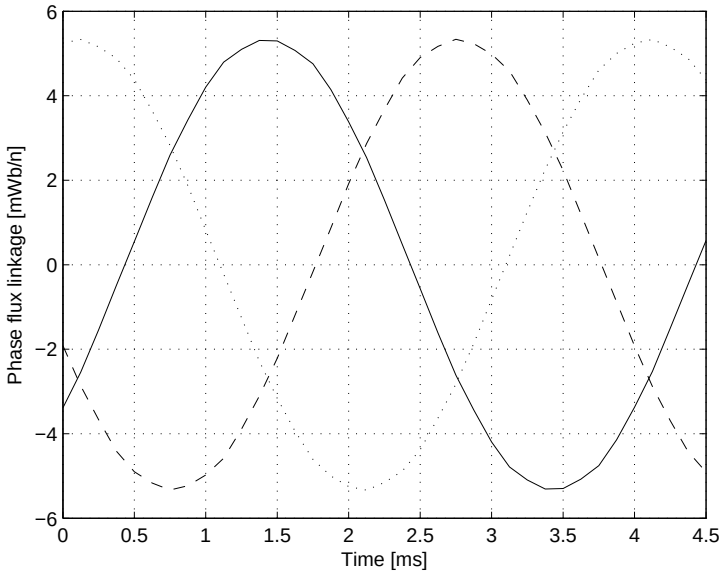

Figure 38: Per turn flux linkage calculated at 3000 rpm.

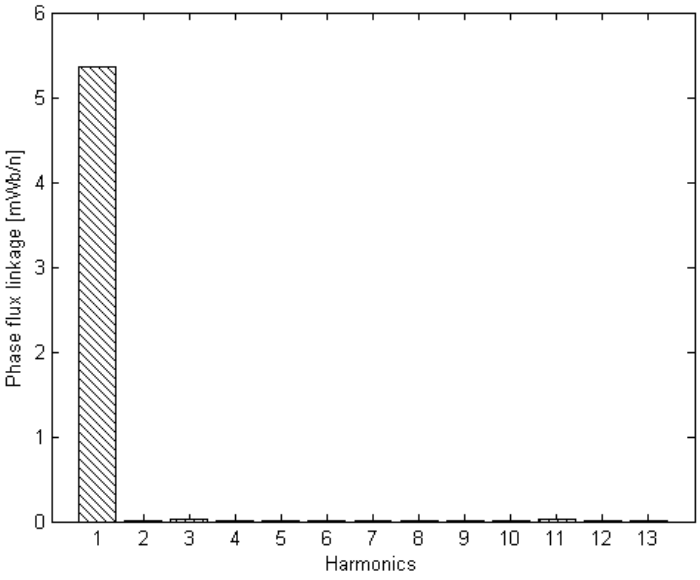

Figure 39: FFT of the flux linkage in Figure 38.

figure, is about 4% of the fundamental.

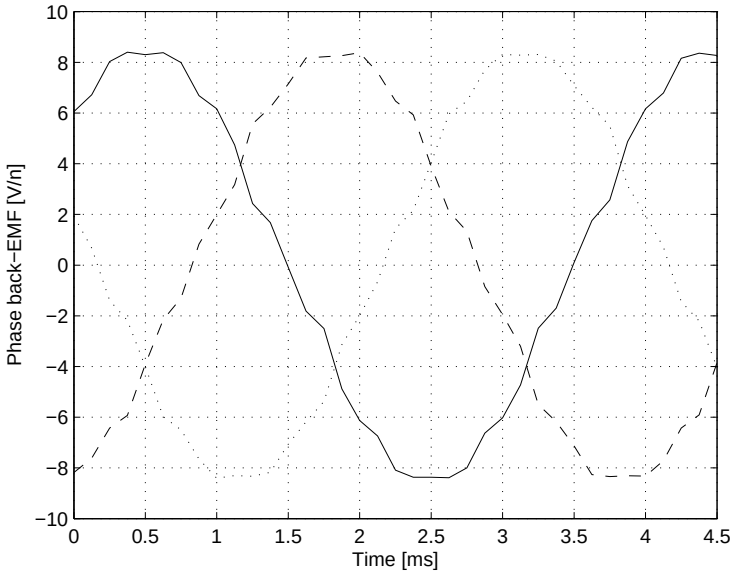

Figure 40: Per turn back-EMF calculated at 3000 rpm.

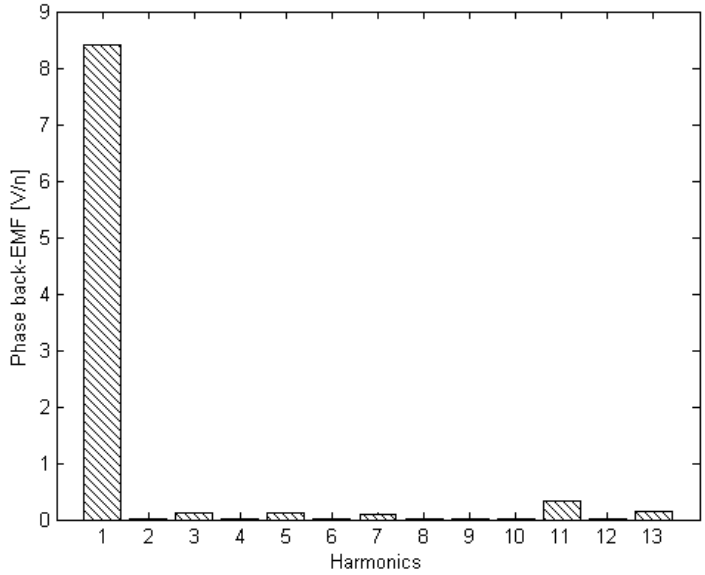

Figure 41: FFT of the back-EMF in Figure 40.

5.4 Computation of the inductances

The direct-axis and the quadrature-axis inductances of a machine with surface mounted magnets and without rotor saliency are often assumed to be equal. This is also the expected result when calculating the inductances without taking into account the magnetic flux due to the magnets or the slightly higher permeability. The method with "demagnetized" or neglected permanent magnets is described in [21]. The FEA result of this method but with the permanent magnets' permeability taken into account is shown in Table 8. One can observe that the inductances in the positive and negative d-direction is about 0.5% higher. This is a consequence of the about 4% higher permeability in the permanent magnets.

The inductances are often considered as non-linear due to saturation of the iron. The level of saturation is determined by the magnitude of the current. However, as seen in Figure 33, the flux from the permanent magnets contributes significantly to the total magnetic flux. In fact, the rotor position (or the current angle) has a clear impact on the inductance, as is shown in Table 9. As expected, the inductance is at its highest in the negative d-direction and at its lowest in the positive d-direction, as the induced flux is counteracting respectively aligning with the flux from the permanent magnets.

Table 8: Inductances with "demagnetized" permanent magnets.

Phase position	**Rotor position** $[mech.degrees]$	**Phase inductance @ 7A/mm²** $[\mu H/n^2]$
-d	67.2	2.30
q	85.2	2.29
+d	103.5	2.30
-q	121.2	2.29

Table 9: Inductances with the magnetic flux due to the permanent magnets taken into account.

Phase position	**Rotor position** $[mech.degrees]$	**Phase inductance @ 7A/mm²** $[\mu H/n^2]$
-d	67.2	2.56
q	85.2	2.14
+d	103.5	1.65
-q	121.2	2.22

5.5 Computation of the torque

5.5.1 Average and ripple

The average torque produced by the machine when applying the nominal current, 53.5 A, at nominal speed, 2400 rpm, is 80.76 Nm, see Figure 42. The torque ripple band is visualized by the dotted lines at 78.38 Nm and 83.23 Nm, which gives a peak-to-peak value of 4.85 Nm. This corresponds to 6% of the average torque.

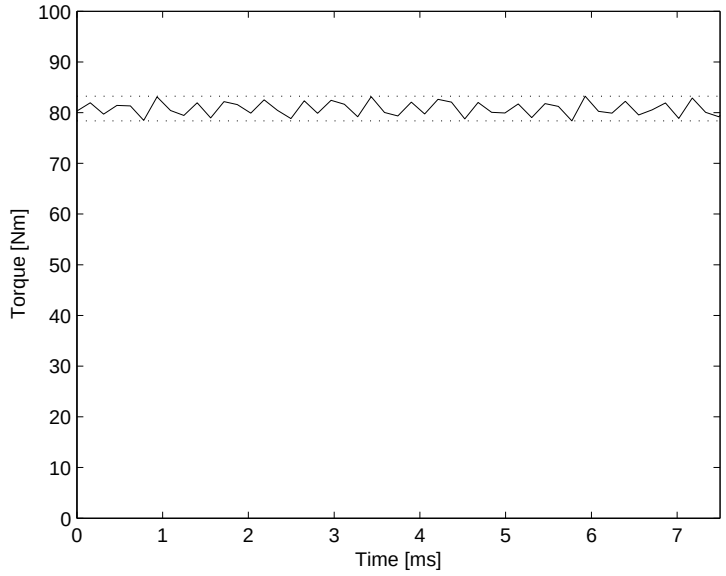

Figure 42: Torque production at nominal speed and nominal current.

5.5.2 Cogging torque

The cogging torque is the torque that one can feel when an unplugged BLDC or PMSM shaft is rotated by hand. It is a consequence of the fact that the magnetic energy that is stored in the air gap changes depending on the rotor position. For some positions the reluctance of the magnetic circuit is minimized and the energy thereby minimized. To reach the next minimum the energy in the air gap must be increased before it drops again. The characteristic of the cogging torque is therefore an alternating torque and its average value ideally sums up to zero.

One period of the cogging torque is plotted in Figure 43. Its peak value is 1.32 Nm which is about 1.6% of the average torque.

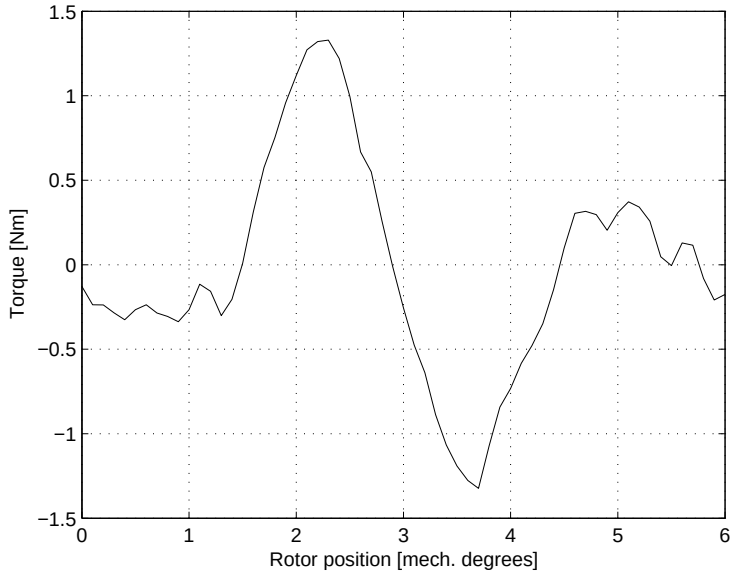

Figure 43: Cogging torque.

5.5.3 Overload and the spacing between the stator shoes

As mentioned in section 2.1.3, most electric machines are able to manage a short time overload which can be several times the rated load. The spacing between the stator segment shoes is expected to affect the overload capacity, since greater spacing prevents the flux leakage between the shoes.

The short time overload is therefore investigated for up to five times the nominal current and for two values of the spacing between the stator segments. The difference in torque for the nominal current is negligibly small, as can be seen in Figure 44. When the current is increased to two times the nominal current, the difference is around 5 Nm. For higher currents, the difference is then increased to around 8 Nm and remains constant within the investigated range.

When the machine is fed by two times the nominal current, the torque is increased by 62% for the assumed spacing of 4 mm. If the spacing is increased to 6 mm the machine will produce 64% more torque than rated, when it is fed by two times the nominal current. It was previously shown in Figure 33 that the magnetic flux density was increased from 1.4 T to 1.7 T when comparing the open circuit flux density and the nominal current flux density. As the iron is almost fully utilized already at rated load conditions, there is simply

not much capacity left for an overload.

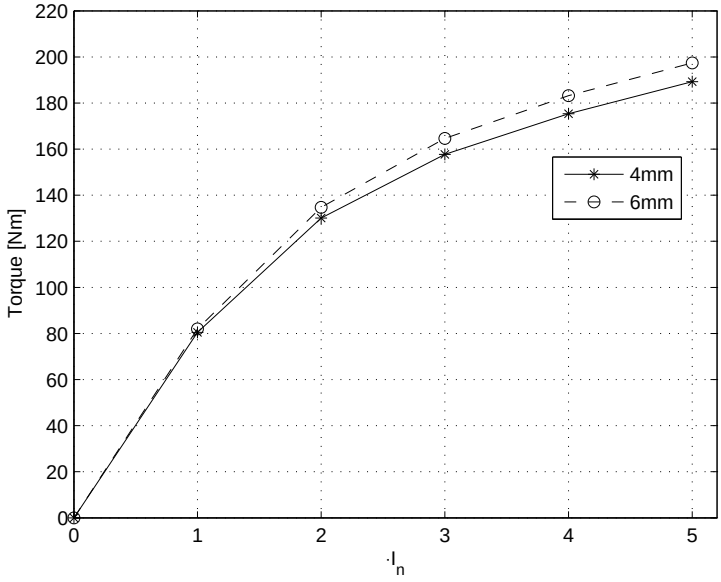

Figure 44: Overload for up to 5 times the nominal current and for a spacing of 4 mm and 6 mm respectively between the stator shoes.

The spacing between the stator segment shoes is varied in four steps to investigate how it affects the torque. The result is shown in Figure 45; an increase from 4 mm to 7 mm gives a 2.6% higher average torque while the torque ripple is incresed by 70%.

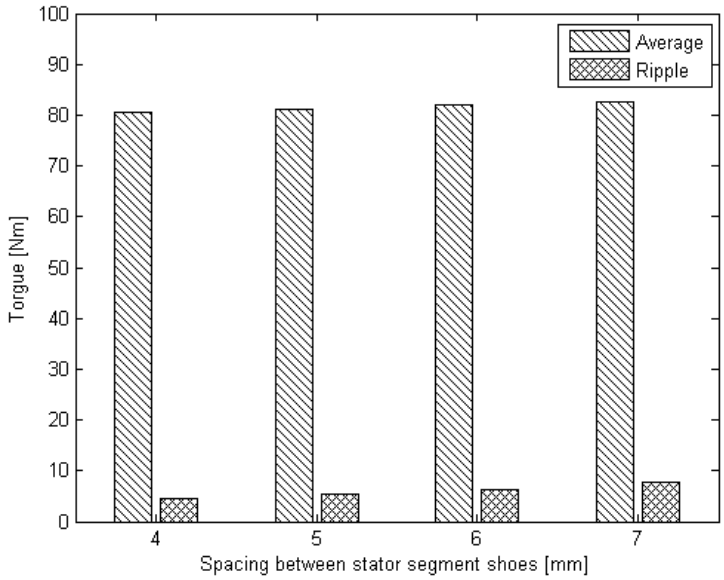

Figure 45: Average and ripple torque when the spacing between the stator shoes is varied.

5.6 Losses and efficiency

The machine characteristic, in terms of torque production, copper and iron losses, is calculated in 30 operation points. The operation points are selected using current steps corresponding to 25% of the rated current and speed steps of 800 rpm. Both copper and iron losses are then interpolated between the calculated operation points, which are plotted as the black dots in the following figures.

When calculating the copper losses, the resistivity of copper has been put to $2.39 \cdot 10^{-8}$ Ωm corresponding to a temperature of 120°C. The expected square relation between current and copper losses can be seen as the square relation between torque and copper losses in Figure 46, since the torque is proportional to the current. As mentioned previously, the frequency depending part of the copper losses such as: proximity effect, induced eddy currents and skin effect are not included, since the windings are modeled as stranded conductors. Therefore, the expected speed dependence cannot be seen in the copper losses shown in Figure 46.

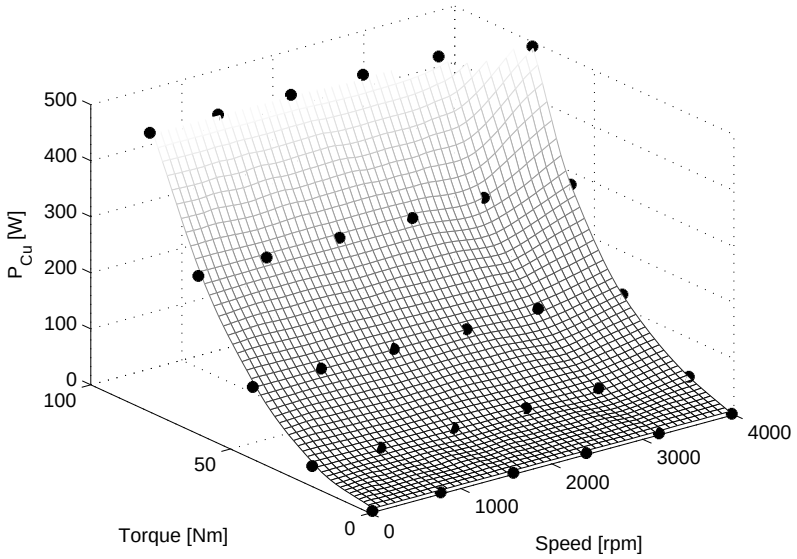

Figure 46: Copper losses.

The calculated iron losses together with the interpolation are shown in Figure 47. It can be seen in the figure that the iron losses depend upon both torque and speed. This since the magnitude of the current affects the flux density and the electric frequency is proportional to the speed. A more distinct square relation between iron losses and electric frequency than in Figure 47 may be expected. For the selected number of turns, the machine is in field weakening operation for speeds above 2400 rpm. The magnetic flux density is thereby decreased for higher speeds and the rise in iron losses reduced.

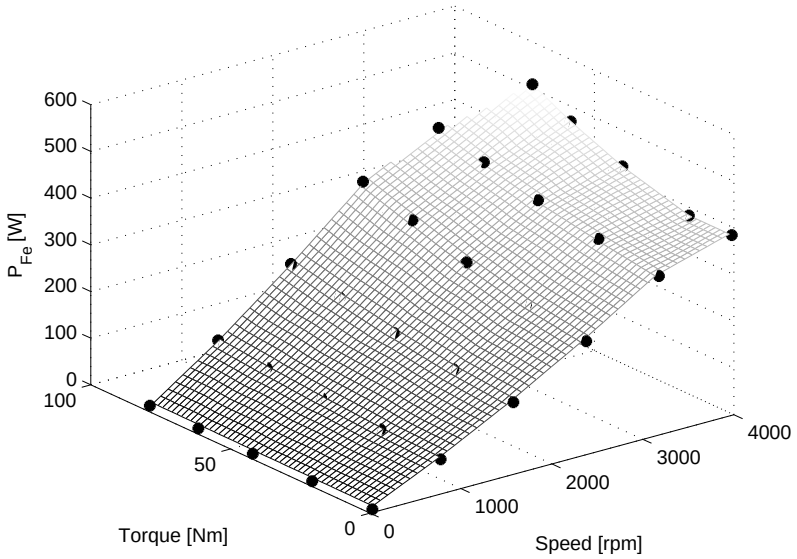

Figure 47: Iron losses.

The iron losses and the copper losses are added together to calculate the machine efficiency, which is shown in the contour plot in Figure 48. For the rated speed and the rated torque operation point, the efficiency is 96%.

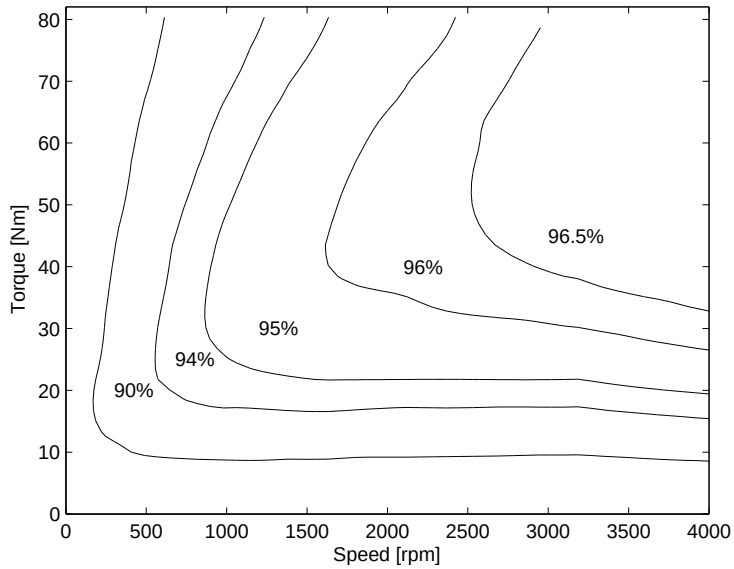

Figure 48: Calculated efficiency map, copper and iron losses taken into account.

6 Discussion, conclusion and future work

6.1 Discussion

The chosen ratio between outer and inner diameter, λ, is based on other existing machine designs. It is probable that it could be tuned to slightly increase the power and torque production. As the outer diameter was limited by the available space, the inner diameter could have been varied to find an optimum using FEA. However, this would have been very time-consuming, as variation of the inner diameter affects other geometric variables; it was therefore not considered in this thesis.

SMC material for the stator segments was chosen to maximize the power and torque production by maximizing the active area of the air gap only, since the electric frequency was too low to take advantage of the lower iron losses at higher frequencies. Another way of reaching maximal power and torque production could have been to not maximize the active area but instead choose laminated steel due to an expected wider linear region before its non-linear region up to saturation. As shown in Figure 30 in section 5.1.3, the presented SMC materials enter their non-linear region already at flux densities of 1.2-1.4 T. When using laminated steel, the overload capacity is also expected to be higher up to a few times the nominal current and then saturate more distinctly compared to the SMC, which was shown in Figure 44 in section 5.5.3.

In section 4.3, the number of turns was chosen to n=30 which does not strictly give the highest possible power and torque production according to the objective in section 1.3. In this case, the significant current increase (for n=20) and the overall performance of the machine are given priority.

The machine volume is 3.8 liters and the weight, considering the active parts only, is 14.8 kg. Using the average torque of 80.76 Nm and the nominal speed of around 2400 rpm, the torque density is calculated to 5.5 Nm/kg and the power density to 5.3 W/cm^3. Both values should be considered carefully as both the torque density and power density are at this stage calculated without feedback from thermal analysis. They are therefore presented only to point out their order of magnitude and not used for any comparison with other machines.

6.2 Conclusion

In this master thesis, the YASA topology was chosen as the most suitable axial flux machine topology to meet the very demanding combination of requirements indicated. The design process has been carried out by using analytic calculations and FEA alternately, focusing on the FEA. As thermal analysis was out of scope for this thesis, the assumed magnetic flux and current densities have been the limiting factors. Using the presupposed values of 1.7 T and 7 A/mm^2, the nominal torque has been determined to about 80 Nm. Considering the weight of the active parts only, this corresponds to a torque density of 5.5 Nm/kg.

The machine torque speed characteristics have been investigated based on the number of turns of the windings. The selected torque speed characteristic, using a DC-link voltage of 500 V and n=30, gives a power density of 5.3 W/cm^3. More information about the expected operation of the machine and the rating of the inverter can be used to make a more appropriate choice of the number of turns to optimize the whole drive system.

It has been shown that the optimization of the rated torque influences the efficiency of the machine; the efficiency for rated torque at rated speed is 96%. The optimization of the rated torque also affects the short time overload capacity of the machine, due to the high level of flux density already required. It is then possible that the amount of iron should be increased and the copper reduced. Thereby the efficiency and the short time overload capacity can be improved at the cost of a lowered rated torque.

6.3 Future work

Calculations considering thermal coupling in the FEA would be a more accurate strategy for finding the thermal limit of the machine together with a cooling system. It is then probable that the assumed current density of 7 A/mm^2 will be altered since it is directly related to the thermal limit. The assumed magnetic flux density of 1.7 T on the other hand is more related to the non-linear behavior of the iron, but an altered value could also be of interest for adjusting the iron losses.

It could also be of interest to calculate the demagnetization current, the maximum current that can be applied to the machine without risk of losing the magnetization of the PMs. It may be a good idea to perform this calculation when the temperature in the machine is known, as the demagnetization field

strength of the PMs is related to their temperature [22].

Depending on the material of the machine casing, the machine geometry might have to be slightly further decreased to introduce a "magnetic insulation" that prevents magnetic flux leakage to the casing. The size of this barrier probably has an impact on the short time overload capacity of the machine.

It is also recommended that the shape of the stator segment shoes be further investigated. Its geometry has been assumed based on existing designs of YASA machines. In section 5.5.3, the spacing between the stator segment shoes was investigated but their axial length has not been evaluated.

Other limits which have not been considered are mechanical strength and fabrication. This could be of particular interest regarding the stator segment shoes but also the permanent magnets, as the shapes of their edges and corners may be unnecessarily sharp in the presented design.

The chosen pole pair and stator segment combination, $p/N_s = 5/12$, is also related to the mechanical strength. As an example, the axial length of the rotor cores , l_r in (34), could be reduced for a higher number of poles. The stator segments could then be made longer and the electric loading and thereby the torque be increased. It must then be investigated how small the parts could be made and yet be able to withstand the greater forces.

References

[1] Council Directive 85/3/EEC of 19 December 1984 on the weights, dimensions and certain other technical characteristics of certain road vehicles, OJ L 2, 3.1.1985, p. 1418 (DA, DE, EL, EN, FR, IT, NL) , Celex document number 31985L0003, Available at http://eur-lex.europa.eu/

[2] Fei, W.; Luk, P.; Jinupun, K.; , "A new axial flux permanent magnet Segmented-Armature-Torus machine for in-wheel direct drive applications," Power Electronics Specialists Conference, 2008. PESC 2008. IEEE , vol., no., pp.2197-2202, 15-19 June 2008

[3] Cirani M. & Lindström J. "Electric hub wheel motors: An initial study for long haul applications" Technical report, Volvo 3P, 2009

[4] Landfors P. & Unfors F. "A concept study of electrical wheel motors for the front axle of a semi truck tractor", Chalmers University of Technology, Göteborg, 2010

[5] Gieras J.F.; Kamper M.J. and Wang R-J. "Axial Flux Permanent Magnet Brushless Machines 2nd Edition" Springer Science & Business Media B.V. 2008

[6] Hendershot J.R. & Miller TJE "Design of brushless permanent-magnet motors" Magna Physics Publishing and Clarendon Press, Oxford 1994

[7] Cirani M. "Analysis of an innovative design of an axial flux Torus-Machine", Roal Institute of Technology, Stockholm 2002

[8] Pillay, P.; Krishnan, R.; , "Application characteristics of permanent magnet synchronous and brushless DC motors for servo drives," Industry Applications, IEEE Transactions on , vol.27, no.5, pp.986-996, Sep/Oct 1991

[9] Woolmer, T.J.; McCulloch, M.D.; , "Analysis of the Yokeless And Segmented Armature Machine," Electric Machines & Drives Conference, 2007. IEMDC '07. IEEE International , vol.1, no., pp.704-708, 3-5 May 2007

[10] Surong Huang; Aydin, M.; Lipo, T.A.; , "TORUS concept machines: pre-prototyping design assessment for two major topologies," Industry Applications Conference, 2001. Thirty-Sixth IAS Annual Meeting. Conference Record of the 2001 IEEE , vol.3, no., pp.1619-1625 vol.3, 30 Sep-4 Oct 2001

[11] Aydin, M.; Surong Huang; Lipo, T.A.; , "Design and 3D electromagnetic field analysis of non-slotted and slotted TORUS type axial flux surface mounted permanent magnet disc machines," Electric Machines and Drives Conference, 2001. IEMDC 2001. IEEE International , vol., no., pp.645-651, 2001

[12] Kano, Y.; Tonogi, K.; Kosaka, T.; Matsui, N.; , "Torque-Maximizing Design of Double-Stator, Axial-Flux, PM Machines Using Simple Non-Linear Magnetic Analysis," Industry Applications Conference, 2007. 42nd IAS Annual Meeting. Conference Record of the 2007 IEEE , vol., no., pp.875-881, 23-27 Sept. 2007

[13] Soong, W.L.; Miller, T.J.E.; , "Theoretical limitations to the field-weakening performance of the five classes of brushless synchronous AC motor drive," Electrical Machines and Drives, 1993. Sixth International Conference on (Conf. Publ. No. 376) , vol., no., pp.127-132, 8-10 Sep 1993

[14] Mohan N.; Undeland T.M. and Robbins W.P "Power Electronics - Converters, Applications and Design" John Wiley & Sons, Inc. 2003

[15] Jiabin Wang; Howe, D.; , "Tubular modular permanent-magnet machines equipped with quasi-Halbach magnetized magnets-part I: magnetic field distribution, EMF, and thrust force," Magnetics, IEEE Transactions on , vol.41, no.9, pp. 2470- 2478, Sept. 2005

[16] Furlani E.P. "Permanent magnet and electromagnetical devices" Elsevier Inc. 2001

[17] Lin, D.; Zhou, P.; Fu, W.N.; Badics, Z.; Cendes, Z.J.; , "A dynamic core loss model for soft ferromagnetic and power ferrite materials in transient finite element analysis," Magnetics, IEEE Transactions on , vol.40, no.2, pp. 1318- 1321, March 2004

[18] Parviainen A. "Design of Axial-Flux Permanent-Magnet Low-Speed Machines and Performance Comparison Between Radial-Flux and Axial-Flux Machines" Lappeenranta University of Technology, Lappeenranta 2005

[19] Surong Huang; Jian Luo; Leonardi, F.; Lipo, T.A.; , "A comparison of power density for axial flux machines based on general purpose sizing equations," Energy Conversion, IEEE Transactions on , vol.14, no.2, pp.185-192, Jun 1999

[20] EL-Refaie, A.M.; , "Fractional-Slot Concentrated-Windings Synchronous Permanent Magnet Machines: Opportunities and Challenges," Industrial Electronics, IEEE Transactions on , vol.57, no.1, pp.107-121, Jan. 2010

[21] Bianchi N. "Electrical machine analysis using finite elements" Taylor & Francis 2005

[22] Arnold magnetic technologies "N35EH datasheet" Available at http://www.arnoldmagnetics.com